Journal of Materials Chemistry A

Accepted Manuscript

ROYAL SOCIETY OF CHEMISTRY

www.rsc.org/materialsA

Heterostructured Cu_2O/CuO decorated with nickel as a highly efficient photocathode for photoelectrochemical water reduction

Amare Aregahegn Dubale[1,†], Chun-Jern Pan[1 †], Andebet Gedamu Tamirat[1], Hung-Ming Chen[1], Wei-Nien Su[2,*], Ching-Hsiang Chen[2,*], John Rick[1], Delele Worku Ayele[1], Belete Asefa Aragaw[1], Jyh-Fu Lee[3], Yaw-Wen Yang[3] and Bing-Joe Hwang[1,3*]

[1] NanoElectrochemistry Laboratory, Department of Chemical Engineering, National Taiwan University of Science and Technology, Taipei 106, Taiwan.

[2] NanoElectrochemistry Laboratory, Graduate Institute of Applied Science and Technology, National Taiwan University of Science and Technology, Taipei 106, Taiwan.

[3] National Synchrotron Radiation Research Center, Hsinchu 30076, Taiwan.

[†] These authors contribute equally

* Corresponding authors: bjh@mail.ntust.edu.tw; wsu@mail.ntust.edu.tw; bluse@mail.ntust.edu.tw

Abstract:

Here we report the design, synthesis and characterization of a novel Cu_2O/CuO heterojunction decorated with nickel cocatalyst as a highly efficient photocathode for solar hydrogen production. The heterojunction structure was shown and examined by X-ray absorption spectroscopy, X-ray photoelectron spectroscopy (XPS), Raman Spectroscopy and Tip-enhanced Raman spectroscopy (TERS). Due to the heterojunction synergism, the Cu_2O/CuO gave a remarkably improved photocurrent density (–2.1 mA/cm^2), i.e. 3.1 times higher than a Cu_2O photoelectrode. Additionally, the Cu_2O/CuO heterojunction, when decorated with nickel cocatalyst, showed six-fold and two-fold increases in photocurrent density (–4.3 mA/cm^2) respectively when compared to Cu_2O and bare Cu_2O/CuO at 0 V vs. RHE under AM 1.5 illumination (100 mW/cm^2). Interestingly, the Ni decorated Cu_2O/CuO photocathode showed an impressive solar conversion efficiency of 2.71% at –0.4 V vs. Pt, i.e. 467% higher compared to bare Cu_2O/CuO. After 20 minutes of standard solar illumination, 87.7% initial photocurrent density was remained for the nickel decorated Cu_2O/CuO heterojunction. This is more than 1.5 times that of bare Cu_2O/CuO (53.6%), suggesting surface modification with Ni not only effectively promotes water splitting but also stabilizes the photoelectrode. The enhanced

photoelectrochemical performance is attributable to the efficient charge transfer and protective role of Ni, the improved crystallinity and the synergism effect of the heterojunction in light absorption and charge separation. This inexpensive photocathode with increased photocurrent density and photostability offers a higher promise for solar hydrogen production.

Keywords: Photoelectrochemical water splitting, Cu_2O/CuO, heterojunction, nickel, cocatalyst, photocathode, hydrogen production

1. Introduction

Due to global warming, finite fossil fuel resources and the exponential increase in world population, the need to develop renewable resources is being brought into ever sharper focus. One almost unlimited renewable energy resource is the sunlight reaching the earth's surface.[1] Converting incoming photons from the sun into storable chemical energy, such as hydrogen, is an attractive 'alternative' way to alleviate existing energy related problems that has attracted much attention.

Currently, many processes e.g. steam reforming,[2-4] coal gasification,[5] biomass derivatives,[6] thermochemical[7] and biological processes[8] are being explored with the goal of generating hydrogen for world consumption. However, most of these processes require a lot of energy and generate a significant carbon footprint. An alternative way to produce hydrogen is to use solar energy to carry out a water splitting reaction. Photoelectrochemical (PEC) water splitting is a potential route towards environmentally friendly hydrogen production as it requires only semiconductor electrodes, water, and sunlight.[9] Semiconductor materials with favorable band alignments for water reduction/oxidation, narrow band gaps and stability under reaction condition are promising candidates for solar energy harvesting – thus, InP,[10] GaP,[11] Si,[12, 13] $CuGaSe_2$,[9] CdTe[14] and WSe_2[15] already find application as hydrogen generating water reduction photocathode materials. However, availability, cost and synthesis procedures still pose severe limitations to their use.[12] Cu_2O, is a non-toxic p-type semiconductor with a direct band gap of 2.0 eV and high theoretical photocurrent density of –14.7 mA/cm^2,[16] that has attracted much attention for use in solar H_2 generation from water, [17, 18] lithium ion batteries [19, 20] and for the degradation of organic dyes under visible light.[21, 22] In addition, copper is inexpensive and naturally abundant and thus offers the potential for cost-competitive large-scale Cu_2O photoelectrode fabrication.[23] However, poor photostability in aqueous electrolytes combined with fast recombination of minority carriers still severely limits the practical utilization of Cu_2O in solar hydrogen production.

Recently, several reports have purported to show various ways of overcoming the above problems associated with Cu_2O. For instance it has been reported that photocorrosion inhibition

and photostability improvements have been achieved by loading cocatalytic Pt, RuO_x and MoS_{2+x} on the thin-film hetrostructured surfaces, obtained from layer-by-layer deposition of n-type semiconductors with more positive conduction bands (e.g. ZnO, TiO_2) than Cu_2O.[17, 18, 24] Coating Cu_2O nanowire arrays with a thin protective graphene layer[25] and carbon layer[26] could also offer a promising way to combat the Cu_2O photocorrosion problem. Furthermore, *in situ* spin coating of the metal oxide co-catalyst ($NiO\text{-}Ni(OH)_2$)[27] on pre-synthesized Cu_2O has also resulted in enhanced photostability and reduced recombination losses.

To-date, due to synthetic method limitations, little research has been carried out on the fabrication and cocatalytic surface activation of Cu_2O/CuO based nanostructures. CuO is a promising p-type semiconductor with a narrow band gap i.e. 1.3 eV to 1.8 eV with strong absorption in the solar spectrum region.[28] In addition, CuO has been used as a component to build heterojunction photoelectrodes with other semiconductors, e.g. ZnO[29, 30], while the high conductivity of CuO makes it a good candidate for clean solar energy applications. [31, 32] Since the conduction band minimum (CBM) of Cu_2O is a little higher than the CBM of CuO; and the valance band maximum (VBM) of CuO is lower than the VBM of Cu_2O, it is reasonable to expect CuO to have electron accepting properties for the Cu_2O/CuO hetrostructure. This suggests that the Cu_2O/CuO heterojunction should have valuable applications in electronics, optoelectronics and in many other nanotechnology fields.

Copper oxides (Cu_2O or CuO) can be synthesized using a number of methods, e.g. metalorganic chemical vapor deposition (MOCVD/CVD),[33-35] electrodeposition,[36, 37] sputtering,[38, 39] and template-based sol–gel approaches.[40, 41] However, none of these methods are suitable for the preparation of Cu_2O/CuO hetrostructures for water splitting. A few groups have recently attempted to synthesize Cu_2O/CuO hetrostructures: for instance, Huang *et al*., found that Cu_2O/CuO heterojunctions can be prepared on a gold substrate by the electrodeposition of Cu nanowires using anodic aluminum oxide (AAO) templates, followed by the thermal oxidation of the Cu nanowire.[32] In another recent study, Wang *et al*., synthesized Cu_2O/CuO heterojunctions on copper foil by embedding anodized Cu_2O thin films with CuO nanowires.[42] Despite this progress, maintaining photoelectrode stability remains challenging; while additionally, existing synthesis strategies require templates, high vacuum conditions, higher potentials and longer

deposition times from aqueous and non-aqueous electrolytes containing hydroxide, chloride and/or fluoride ions at room temperature. As a result, a facile, scalable, template free, cheap, and environmentally friendly alternative strategy for fabricating heterostructured Cu_2O/CuO remains elusive.

CuO grown on top of Cu_2O (Cu_2O/CuO) improves the photoresponse of the photoelectrode while also serving as a protective layer against Cu_2O photocorrosion.[31] Other studies have shown a limited Cu_2O/CuO photocathode stability enhancement can be achieved (probably due to self photocorrosion of the CuO layer) during the photocatalytic reaction.[32] Here we also examine the effect of cocatalyst loading on the Cu_2O/CuO heterojunction's surface with respect to its photoelectrochemical (PEC) performance. To the best of our knowledge, this is the first report focused on the effects of cocatalyst loading on the Cu_2O/CuO surface and the fabrication of a Cu_2O/CuO based electrode for water reduction on a conductive substrate (fluorine doped tin oxide). Pt, when deposited on semiconductors, is a well known electrocatalyst; however, Pt is extremely scarce, making it costly to use on a large scale for hydrogen production.[43] A more earth-abundant alternative to Pt is Ni, which has been shown to be an effective co-catalyst for solar-driven H_2 generation when deposited as nanoparticles on a graphene oxide sheet[44], or on crystalline Si electrodes,[45] where mechanistically it is assumed to act as a trap for photogenerated electrons into the electrolyte solution, thereby retarding charge recombination, while also stabilizing the photoelectrode.

In this work, we report a facile synthetic strategy to make Cu_2O/CuO on a fluorine doped tin oxide (FTO) substrate. We prepared the Cu_2O/CuO heterojunction in one-step by oxidizing a Cu film deposited on FTO using an electrolysis method. The process used is simple, facile, scalable, template free, cheap, and environmentally friendly. We investigated the effects of annealing time and oxidation temperature on the crystallinity of heterostructured Cu_2O/CuO – in order to maximize light absorption. The heterostructured Cu_2O/CuO, used as a photocathode for PEC based H_2 production, was examined to evaluate its activity and stability; the presence of the CuO layer was found to enhance the photo-response of the electrode. We also demonstrate for the first time that decorating the Cu_2O/CuO surface with a robust and cheap nickel cocatalyst is a viable strategy for achieving improved photostability and photocurrent density with suppressed

reduction of the photocatode's outer CuO layer. In addition to PEC performance measurements, the heterojunction photocathode was investigated with respect to its stability.

2. Experimental section

2.1 Methods

2.1.1 Synthesis of Cu_2O/CuO. All chemicals used in this study were of analytical grade and used without further purification. Cu films were prepared by electrolysis of $CuSO_4.5H_2O$ (99%, Across Organics) at constant applied potentials. The commercial fluorine-doped tin oxide glasses (FTO 15 Ω, 1.5 cm × 3 cm) were cleaned with isopropyl alcohol, acetone, soapy and pure deionized water for 5 min each in ultrasonication bath and quickly dried in N_2 flow before using. Cu was deposited in a conventional two electrode cell system using a programmable DC power supply. FTO glasses were used as the cathode and anode electrode. The FTO glasses were dipped into electrolyte solution. The FTO connected to the negative and the positive terminals of the power supply were used as cathode and anode respectively. Cu films were deposited from the aqueous solution containing saturated $CuSO_4.5H_2O$ with a potential of 5 V for 2 minutes. The Cu_2O/CuO heterojunction was obtained *in situ* by annealing the as prepared Cu film in a cubic furnace in air. That is, the Cu_2O/CuO heterojunction was prepared by thermal oxidation of the as synthesized Cu film in air at different temperatures varying from of 350 ˚C to 650 ˚C for 4 hour. To investigate the effect of annealing time, the as synthesized Cu film was annealed at temperature of 350 ˚C for 0.5, 1, 2, 3 and 4 hour. For clarity, the Cu_2O/CuO photocathodes prepared at 350, 450, 550 and 650 ˚C for 4 hour are named as Cu_2O/CuO-350, Cu_2O/CuO-450, Cu_2O/CuO-550 and Cu_2O/CuO-650.

2.1.2 Deposition of Ni nanoparticles on Cu_2O/CuO heterojunction. Deposition of nickel nanoparticles on Cu_2O/CuO heterojunction was carried out via the facile hydrothermal route and the spin-coating method. Firstly, nickel nanoparticles were synthesized by the following process. Nickel chloride hexahydrate (0.427 g), sodium hypophosphite (5.27 g) and potassium hydroxide (3.58 g) were dissolved in 64 ml of deionized water. The mixture was vigorously stirred for 30 minutes at room temperature under atmospheric pressure forming suspension solution. The prepared suspension was taken into a Teflon-lined stainless steel with 0.8 filling factor, sealed, and maintained at 200 ˚C for 10 h. After this the autoclave was

naturally cooled to room temperature, the black products were collected, washed with plenty of distilled water and dried at 50 ˚C for 4 hr in the air. Secondly, Cu_2O/CuO heterojunctions obtained at 450 ˚C for 4 hr (hereafter named as Cu_2O/CuO) were decorated by spin-coating an alcoholic solution of as synthesized nickel nanoparticles (0.07 M) onto the surface of Cu_2O/CuO photoelectrode at 1500 rpm for 10 s. By reiterating the above deposition cycle, the desired amount of nickel nanoparticles can be loaded on the Cu_2O/CuO photoelectrode. Now onwards, the Cu_2O/CuO photoelectrode decorated with varying deposition cycle (N= 1, 2, 3, 4 and 5) are named as Cu_2O/CuO/Ni-1, Cu_2O/CuO/Ni-2, Cu_2O/CuO/Ni-3, Cu_2O/CuO/Ni-4 and Cu_2O/CuO/Ni-5 respectively.

2.2 Structure characterization

The photoelectrodes were characterized by XRD, SEM, DRS UV-Vis, Raman, XPS and XANES/EXAFS. X-ray diffraction (XRD) pattern were acquired with a D2 phaser XRD-300 W, with measurements taken using Cu K_α radiation at 40 kV and 100 mA. Spectra were obtained with a linear silicon strip `Lynx Eye' detector from 20˚ to 80˚ at a scan rate of 3˚ min^{-1}. The morphology of the electrodes were characterized using Field Emission Scanning electron microscopy (EDX JSM 6500F, JEOL) The diffuse reflectance UV-vis adsorption spectra were obtained using a JASCO (ISV-469) V 560 UV-Vis spectrometer with fine $BaSO_4$ powder as reference. Raman measurements were performed on a ProMaker confocal Raman microscope system as integrated by Protrustech Co., Ltd. A solid state laser operating at λ= 532 nm was used as the excitation source with a laser power of 20 mW to circumvent degradation with 10 s exposure times and 15 accumulations. X-ray photo-electron spectra (XPS) (PHI, 1600S) were recorded at the National Synchrotron Radiation Research Centre (NSRRC), Taiwan with 24A XPS beam line station. In order to obtain the near field Raman signal on the surface of the Cu_2O/CuO, atomic force microscope (AFM) was applied to combine with microscope Raman spectroscopy. The AFM tip was coated by Au as to enhance the Raman signal as called tip enhanced Raman scattering (TERS). This characterization was performed on 632.8nm laser excited light source UniRAM microscope Raman system (UniNanoTech) combined with MV4000 AFM scanning stage (Nanonics). To prevent degradation, the exposure time was 5 seconds with 10 accumulations. An objective lens 50×/0.55 N.A. was used and the measurement was carried out at room temperature and dark condition. Before measurement the Raman band of

a silicon wafer at 520 cm^{-1} was used as the standard reference to calibrate the spectrometer. The hard X-ray absorption spectra (XAS) were collected at the beam line BL17C1 of National Synchrotron Radiation Research Center (NSRRC) in Hsinchu, Taiwan. The storage ring of the electronic accelerator can supply the electronic energy of 1.5 GeV and the operation current at 360 mA. A Si double crystal monochromator was used to perform energy scan, of which the parallelism can be adjusted to eliminate the high order harmonics. All XAS data were recorded using the fluorescence mode. The Ni content in the residue of the electrolyte was analyzed by using ICP-AES (inductively coupled plasma – atomic emission spectrometry) JY 2000 2 model from HORIBA Scientific.

2.3 Photoelectrochemical measurement

The photoelectrochemical performance of the electrodes was assessed in a three electrode system using an aqueous solution of 1M Na_2SO_4 buffered at pH 5 with potassium phosphate (0.1 M). The three-electrode configuration consists of Ag/AgCl in saturated KCl as reference electrode, a Pt wire as the counter electrode and the prepared Cu_2O/CuO or Cu_2O/CuO/Ni as working electrode. The photoresponse of the synthesized electrode was acquired under chopped illumination from a 300 W Xenon lamp equipped with AM 1.5 filter. The intensity of light source was calibrated with a Si diode (Newport) to simulate AM 1.5 illumination (100 mW/cm^2). For all the samples, a scan rate of 10 mV/s was used for the current versus potential measurements (LSV). Photocurrent stability tests were performed by measuring the photocurrent produced under chopped light irradiation (on/off cycles of 10 s) at a fixed biasing potential of 0 V vs. RHE. During the PEC tests, the electrolyte was constantly purged with N_2 for 30 minutes. The electrochemical impedance spectroscopy (EIS) was performed using an electrochemical impedance analyser with an AC amplitude of 10 mV and frequency range between 100 kHz to 0.1 Hz. The measured EIS data were obtained at an applied bias of 0 V vs. RHE at 25 ˚C.

2.4 Photoelectrocatalytic hydrogen measurement

The photostability measurement equipped with hydrogen quantification experiment on bare Cu_2O/CuO and Cu_2O/CuO/Ni-3 was carried out at an applied potential of 0 V vs. RHE under AM 1.5 irradiation. The evolved gas during the reaction was collected above the water through a tube connected to a separate burette equipped with septum as head cap. The change in volume of water displaced by the generated gas was taken as total volume of evolved gas. The evolved gas

sample was taken from head cap of the burette with a gas-tight syringe and analyzed using a YANGI–LiN gas chromatograph equipped with PDHID detector. Generated H_2 was carried out following the GC calibration curve made with known concentration of H_2 (5% H_2/Ar)

3. Results and discussion

The fabrication of the host substrate (Cu film) on FTO for the growth of the Cu_2O/CuO heterojunction is illustrated in Scheme 1. Fluorine doped tin oxide (FTO) was chosen as a film growing substrate because it is electrically conductive, transparent, highly temperature resistant, chemically inert, relatively stable under atmospheric conditions; additionally, it is less expensive than substrates such as indium tin oxide.[46] A Cu film, uniformly coated on FTO, was first prepared by a simple and facile electrolysis method. A pair of connected FTO films (Scheme 1), immersed in a saturated solution of $CuSO_4$ electrolyte for 2 minutes with 5 V at 25 ˚C, resulted in the formation of a dense layer of a uniform reddish orange colored Cu film over the conductive FTO substrate exhibiting exactly the same natural color as a copper substrate e.g. a Cu foil. During the electrolysis of copper sulphate, using FTO as an inert electrode, it is known that $CuSO_4$ is ionized producing Cu^{2+} and SO_4^{2-} ions ($CuSO_4 \rightarrow Cu^{2+} + SO_4^{2-}$), and in doing so allows the transfer of copper ions, in preference to H^+ ions, from the solution to the cathode. This is probably because the reduction potential of Cu^{2+} is more positive than that of hydrogen ions. The migration of positively charged copper ions to the cathode results in the formation of the reddish orange colored copper sheet on FTO upon gaining pair of electrons at the cathodic surface (according to reaction 1 below).

$$Cu^{2+}_{(aq)} + 2e \longrightarrow Cu_{(s)} \quad (1)$$

At the anode, of the two anions in solution OH^- and SO_4^{2-}, OH^- is discharged first, as confirmed by the evolution of oxygen gas on the FTO's surface, see reaction 2 below. The ions remaining in the solution, H^+ and SO_4^{2-} cause a change in pH from 4 to 1.5. Furthermore, with the complete deposition of Cu^{2+} ions on FTO the same electrolyte solution changes from deep blue to colorless (or pale blue).

$$4\,OH^-_{(aq)} \longrightarrow 2H_2O_{(aq)} + O_{2(g)} + 4e^- \quad (2)$$

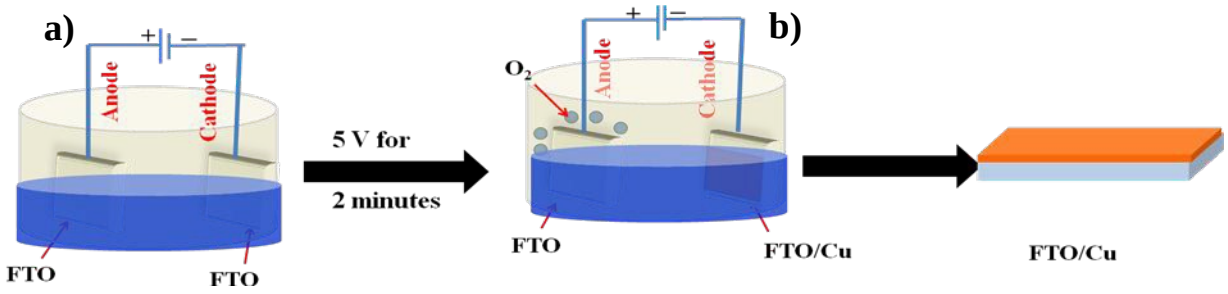

Scheme 1. Synthetic strategy of: (a) electrodeposition of Cu film on FTO using a saturated solution of $CuSO_4$ (b) growing Cu film.

This work focused on the Cu_2O/CuO synergism towards PEC performance. A Cu film on FTO was subjected, in a cubic furnace, to thermal oxidation (in air) for various annealing times (0.5, 1, 2, 3 and 4 hours at 350 ˚C) and annealing temperatures (350, 450, 550 and 650 ˚C for 4 hours) to optimize the reaction conditions. The XRD patterns of the Cu film and thermally oxidized copper at 350 ˚C, in air for different times, are shown in Figure 1(a). Well defined peaks at 42.6, 50.3 and 72.5˚ correspond to diffractions from the (111), (200), and (220) planes of copper (JCPDS card number 04-836, Figure 1(a) red colored curve). This shows that a pure and well crystallized Cu film with no impurities peak, such as cuprous or cupric oxides, was formed on the FTO. This was also confirmed from the X-ray absorption near-edge structure (XANES) and extended X-ray absorption fine structure (EXAFS) characterizations shown in Figures 1(b) and 1(d) respectively. As shown in Figure 1(b), the XANES spectra of the synthesized Cu film is similar to that of the XANES spectra of Cu foil. The Cu-Cu bond length of the Cu film, centered at 2.4 Å in the EXAFS spectra is also in agreement with the Cu-Cu bond length of Cu foil (Figure 1(d)).

Annealing the Cu film at 350 ˚C for durations ranging from 0.5 to 4 hours (Figure 1(a)), revealed changes in composition of the film. In all the cases, annealing the film created new peaks at 36.4, 42.3 and 61.5˚, matching reflections from the (111), (200), and (220) planes of Cu_2O (JCPDS card number 05-0667). It is observed that (Figure 1a) the intensity of Cu_2O along the (111) direction get increasing with increased in annealing time, indicating preferential growth of Cu_2O is along the <111> direction on the FTO substrate. Cu film annealed for 3 hr, or more, showed small new emerging peaks at 35.5, 38.9 and 65.8˚, corresponding to the CuO phase (JCPDS card number 5-661). The appearance of these peaks is clearly shown in Figure S1 (see supporting information). Oxidation of the synthesized Cu films was also investigated using XANES and

EXAFS measurements, see Figures 1(b) and 1(d) respectively. The features of the XANES spectra (Figure 1(b)) show a slight shift in the edge position from the Cu film or Cu foil ref. As can be seen in Figure 1(c) (enlargement of selected portion in Figure 1(b)), the edge position of heat treated Cu film is shifted to higher energy, indicating that oxidation takes place during 350 ˚C treatment. We found that the spectrum of the sample after 4 hr treatment under 350 ˚C is close to that of the Cu_2O reference, indicating the average oxidation of Cu species is close to +1. This is in good agreement with our XRD results. The information from XANES is also supported by the EXAFS spectra given in Figure 1(d). As the annealing time increases, the intensity of Cu metal is supposed to decrease, indicating the increased oxidation of the Cu film. The discrepancy in intensity of Cu during annealing from 2 hr to 3 hr might result from the inhomogeneous sample in XAS measurement, which usually focused only small area of the sample.

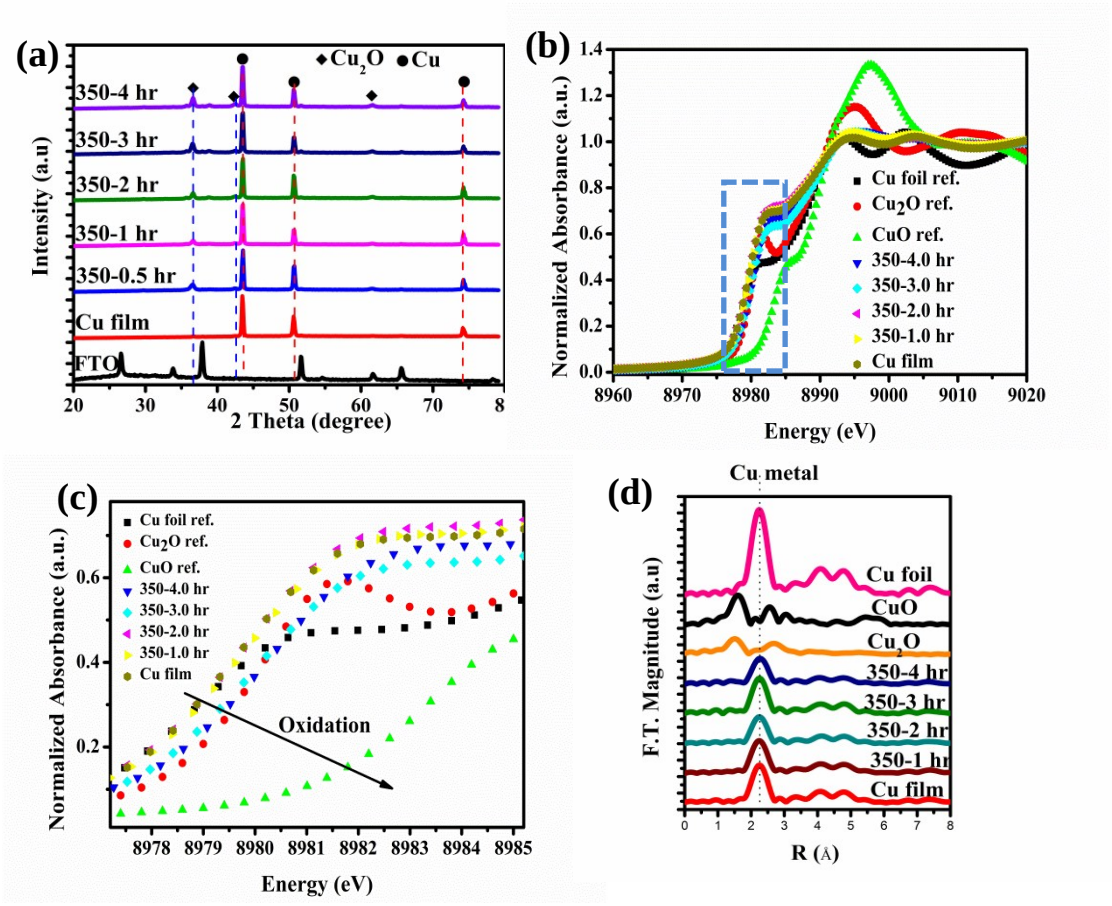

Figure 1. (a) XRD patterns (b) XANES (c) enlargement of selected portion in Figure 1(b) and (d) EXAFS spectra of Cu film and Cu film oxidized at 350 ˚C for 1, 2, 3 and 4 hr.

The surface of the Cu film on the FTO substrate turns black after oxidation, suggesting that the surface oxide is CuO.[47] Further examination under an electron microscope (SEM) revealed a clear morphological difference between the as-synthesized Cu film and films subjected to the thermal treatment. The microstructures of the as-synthesized Cu films before annealing and films annealed at 350 ˚C for 0.5, 1, 2, 3 and 4 hours are displayed in Figure 2. Figure 2(a) shows Field emission SEM images of the Cu film fabricated by the electrolysis method. As shown in the scanning electron microscope (SEM) image in Figure 2(a), the FTO substrate was completely coated with Cu film after it had been immersed in a $CuSO_4$ solution at 5 V for 2 minutes. The film had a reddish orange color, typical of Cu. As clearly seen in the image (Figure 2(a) and Figures S2 a1-a2), the as-prepared Cu film before annealing has a rough surface and irregular grain size. However, when the films were annealed at 350 ˚C for ≥0.5 hour, the morphology showed better uniformity in grain size (Figure 2(b) to 2(f) and Figure S2).

SEM images of a Cu film, after it had been heated in air at 350 ˚C for 0.5 hour (Figure 2(b)), revealed the formation of continuous and homogeneous nanoparticles with little surface remaining uncovered. As seen in Figures 2(c) to 2(f), only small amounts of less packed Cu_2O films were formed at lower temperatures duration annealing. With prolonged calcination times (e.g. for films annealed for 3 and 4 hours, Figures 2(e) and 2(f), respectively), the structure of the films became gradually denser and more closely packed. The images also reveal that increased amounts of films (Cu_2O and CuO) on the FTO substrate were obtained with increasing annealing times. As shown in Figure 2(f), a film oxidized at 350 ˚C for 4 hours shows a smooth surface with well packed small particles with observable small gaps between the nanoparticles (indicated by small circles in the high resolution SEM image Figure S2 f2), possibly due to incomplete grain growth after the oxidation process (see Figure S2). In our study, the results from XRD, XAS, EXAFS and SEM related to the annealing time suggest a promising route for conducting further experiments.

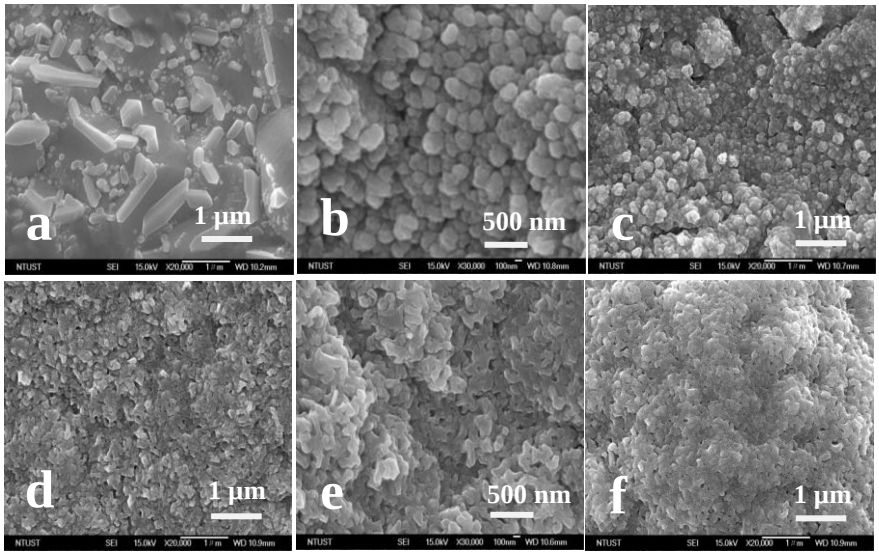

Figure 2. Scanning electron microscopy images of the as-synthesized Cu film (a) and Cu film annealed at 350 ˚C for: 0.5 (b), 1 (c), 2 (d), 3 (e) and 4 hr (f).

We also investigated the effect of the annealing temperature on the growth of heterostructured Cu_2O/CuO. In this study, the as-synthesized Cu films were placed in a cubic furnace and heated for 4 hours at temperatures in the range 350 to 650 ˚C. The surface of the Cu film became blackened with a reddish hue at the back when heated up to 450 ˚C (Figures S3b and 3c) and was totally tarnished, both front and back, at higher annealing temperatures (~650 ˚C) (Figure S3e). These changes probably result from oxidation of the film. Further examination of Cu films (treated at 350, 450, 550 and 650 ˚C) by Field emission scanning microscopy, see Figure 3, shows that film oxidized at 350 ˚C for 4 hours has a smooth surface with well packed small particles and observable small inter-nanoparticle gaps as indicated by small circles in the high resolution SEM image in Figure 3(a), possibly due to incomplete grain growth after the oxidation process. More interestingly, the Cu film oxidized at 450 ˚C (Figure 3(b)) revealed a highly dense, rough surface with a few nanowires emerging from the inner surface of the film (see marked areas in Figures 3(b) and 9(c)) in later section. Similar features (surface roughness) were also revealed by atomic force microscope (AFM) measurements (Figure S4).

Figure 3(c) shows SEM images of the Cu film after it had been heated in air at 550 ˚C for 4 hours. As can be seen in this figure, the surface of the substrate was completely covered by a

compact and uniform film. Unlike the film treated at 450 ˚C, nanowire growth on the surface of the film was totally absent. This is probably because, usually CuO nanowires, which have a high density of Cu at the bottom and low density at the top and a reverse O distribution, were grown either from the middle, or at the bottom of the Cu_2O layer, and the growing direction of nanowires was consistent with the diffusion of Cu.[42, 48]. Thus, in our study, the absence of nanowires on the film's surface for the sample annealed at 550 ˚C is probably due to inhibited growth of CuO nanowires outward from the thicker films. SEM images of the film, annealed at 650 ˚C, in Figure 3(d) reveal formation of a few pits[49] randomly distributed over the compact, flat and homogeneous film surface. The formation of the pits is probably due to plastic deformation caused by film thickness beyond a critical limit,[50] implying the existence of crystal dislocation during film growth.[51]

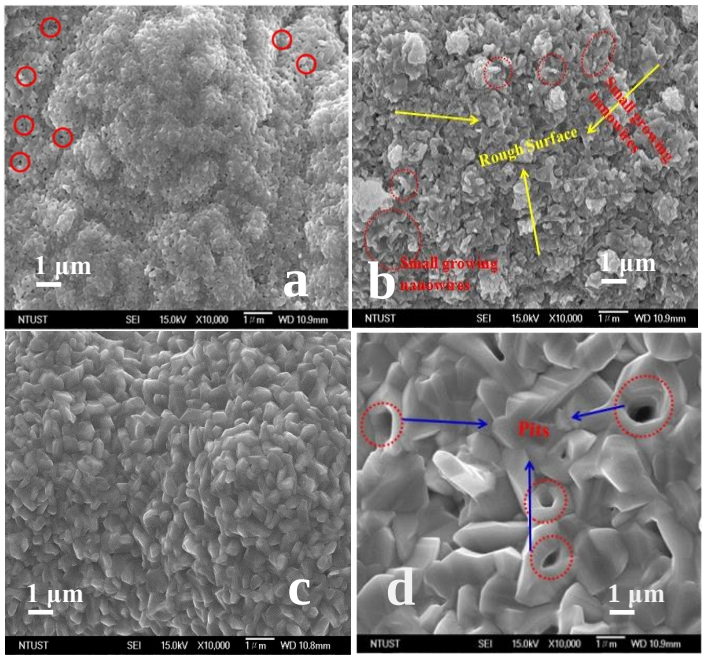

Figure 3. Scanning electron microscopy images of the Cu film annealed at: 350 (a), 450 (b), 550 (c) and 650 ˚C (d).

We further examined the composition, structure, and crystallinity of heterojunctions, obtained at different annealing temperatures; using XRD, Tip-enhanced Raman spectroscopy (TERS) and XAS. The XRD patterns of Cu films annealed at 350 ˚C to 650 ˚C for 4 hours are given in Figure 4(a). As mentioned, the Cu film annealed at 350 ˚C for 4 hours resulted in the formation of relatively intense Cu_2O peaks together with slightly weak emerging CuO peaks. It was found that

the intensity of Cu_2O along the (111) direction increased with the increase of oxidation temperature from 350 ˚C to 450 ˚C (magenta colored curve in Figure 4(a)). The improvement in Cu_2O crystallinity at 450 ˚C, together with the significant intensity of the (111) plane of CuO, confirms the formation of the Cu_2O/CuO heterojunction. However, the monoclinic phase of CuO started to dominate the Cu_2O peak when the annealing temperature increased to 550˚C (Figure 4(a)). The XRD patterns reveal that the characteristic features of the Cu and Cu_2O phases disappear when the annealing temperature increases from 550 to 650 ˚C. This observation indicates the complete conversion of Cu_2O into CuO, due to the higher annealing temperature promoting the oxidation of Cu_2O by diffused oxygen resulting in additional CuO phase, i.e. $2Cu_2O + O_2 \rightarrow 2CuO$ (see further information in supportive information).[52] The phase transformation of Cu film and the effect of the annealing temperature were also studied by Raman spectroscopy. Figure 4(b) shows the Raman spectra of Cu films annealed at 350, 450, 550 and 650 ˚C. The presence of peaks at 218 cm^{-1} and 635 cm^{-1} (shown by diamonds in Figure 4(b)) is indicative of the existence of the Cu_2O phase.[25] The peak at 218 cm^{-1}, originating from the second-order Raman-allowed mode of Cu_2O, was relatively stronger with 450 ˚C treatment and then gradually disappeared as the annealing temperature increased. The strong peak feature demonstrates that better crystallization of Cu_2O in the heterojunction can be achieved with an annealing temperature of 450 ˚C, which is consistent with the XRD results. On the other hand, both Cu_2O and CuO were observed for Cu film annealed at 350, 450 and 550 ˚C; however, the Cu film annealed at 650 ˚C revealed only the CuO phase. As the annealing temperature increases, the characteristic CuO peak, usually centered at 298 cm^{-1} for pure CuO, shifts slightly (low Raman shift), probably because stress and non-stoichiometry affect the peak position and the width at the peak's half maximum height.[53] The formation of a pure CuO phase at 650 ˚C also confirms the complete conversion of metallic copper and Cu_2O film into the CuO phase. This is probably because once the metallic Cu is consumed, the outward diffusion of Cu^{2+} comes to an end and the whole film becomes pure CuO phase due to the proximity of ambient O_2 to film.[54] The complete consumption of metallic copper was also confirmed by XRD results.

The effective oxidation of the Cu film during annealing at different temperatures is also shown by the XANES spectra (Figure 4(c)). Figure 4(d) shows portions of the enlarged XANES spectra in Figure 4(c). For brief comparison we have shown the X-ray absorption near-edge structure

(XANES spectra) of Cu_2O, CuO and Cu foil references representing the absorbance peaks of Cu^+, Cu^{2+} and Cu respectively. The edge position of Cu is shifted to higher energy (in the direction shown in Figure 4(d)), indicating that further oxidation takes place while the temperature increases. The position of Cu after 4 hr treatment under 650 ˚C is close to that of the CuO, indicating the average oxidation of Cu is close to +2. From the enlarged XANES spectra (Figure 4(d)), Cu film annealed at 350 ˚C and 450 ˚C has a similar feature to the Cu_2O reference sample (Cu_2O ref), while Cu films annealed at 550 ˚C and 650 ˚C share more features in common with that of the CuO reference sample, indicating that lower and higher annealing temperatures resulted in more Cu_2O and CuO like components, respectively. The shift in edge position to higher energy after annealing clearly implies that heat treatment changes the Cu film's oxidation state.

We also studied the variation of Cu film structures with the annealing temperature by extended x-ray absorption fine structure (EXAFS), Figure 4(e). Based on the radial distribution functions obtained by Fourier Transformation, Cu film annealed at 350 and 450 ˚C revealed similar EXAFS spectra to the Cu_2O reference. On the other hand, Cu film annealed at relatively higher temperatures (550 and 650 ˚C) exhibited similar EXAFS spectra to the CuO reference. If we compare their spectra with the spectrum of the synthesized Cu film or Cu foil, it can be seen that the intensity of Cu–Cu bonding diminishes as the annealing temperature increases. This provides supplementary evidence that annealing the Cu film leads to dramatic changes in the oxidation state. More interestingly, the spectra of Cu films annealed at 450 and 650 ˚C, resemble those of the Cu_2O and CuO references, suggesting Cu_2O and CuO respectively are the major species at these temperatures. These results support our XRD characterization.

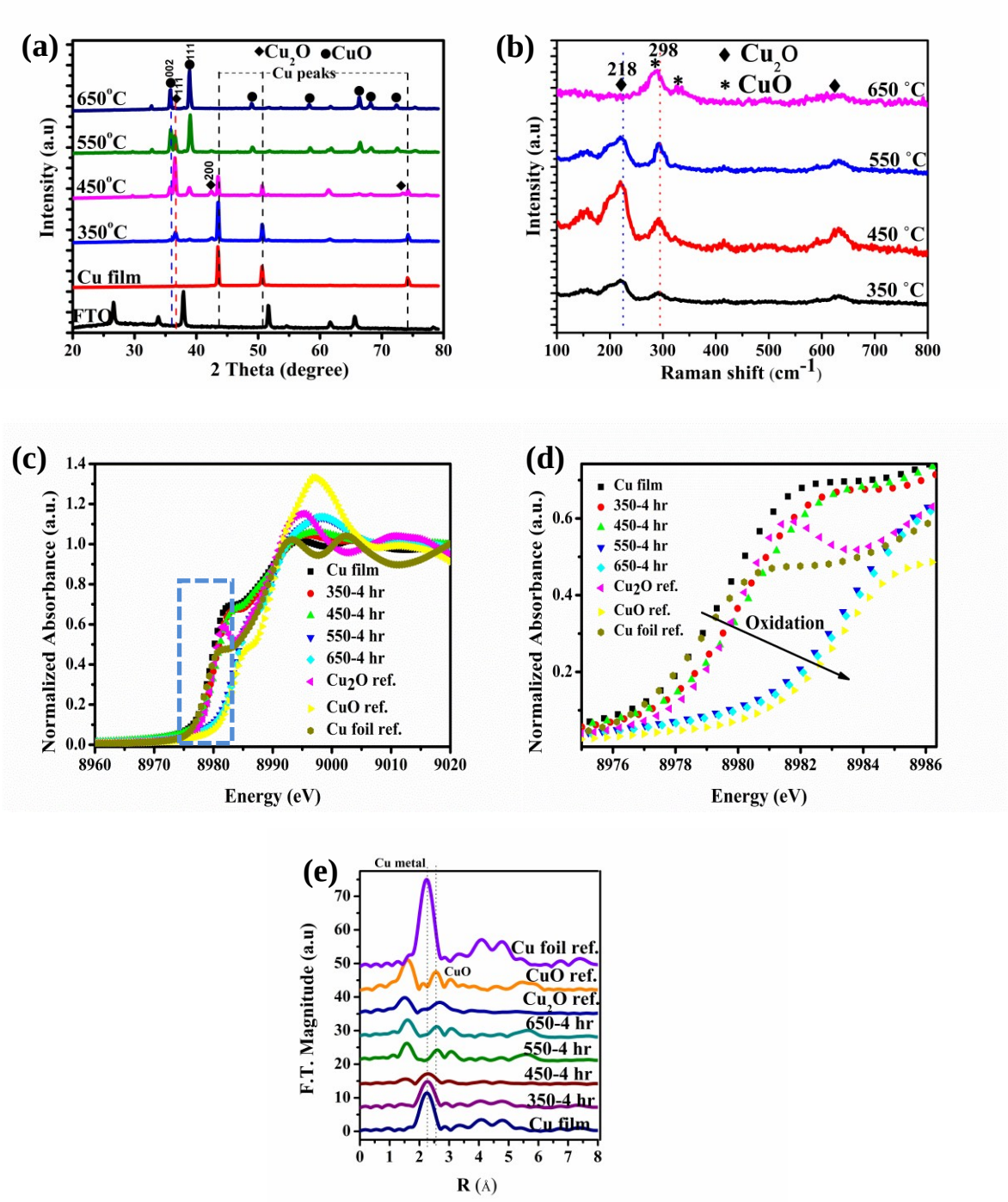

Figure 4. (a) XRD patterns (b) Raman spectra, (c) XANES spectra (d) enlargement of selected portion in Figure 4(d) and (e) EXAFS spectra of Cu film oxidized at 350, 450, 550 and 650 ˚C.

To gain more insight into the chemical composition of the photoelectrode, we also carried out XPS measurements on Cu_2O/CuO fabricated at 450 ˚C. The Cu 2p peak XPS spectrum of Cu_2O/CuO is shown in Figure 5(a); the two peaks centered at 933.5 and 953.2 eV were assigned to Cu 2p3/2 and Cu 2p1/2 of CuO, respectively, and the two smaller peaks, obtained by deconvoluting the major peaks, appearing at 932.4 and 952.2 eV correspond to Cu_2O. The presence of two extra shake-up satellite peaks at relatively higher binding energies, 942.9 and 954.2 eV, also indicate the existence of CuO on the surface. The curve-fit results of the Cu 2p core level XPS measured on the surface of the Cu_2O/CuO photocathode reveal that the predominant phase was CuO, constituting about 64% on the surface of the film annealed at 450 ˚C.

We investigated the chemical composition of the photoelectrode, Cu_2O/CuO fabricated at 450 ˚C, with tip enhanced Raman spectroscopy (TERS) using a 632.8 nm wavelength laser as the excitation source. Figures 5(b) shows TER spectra of the Cu_2O/CuO heterojunction at tip in and tip out conditions. Figure 5(c) shows the TER spectrum, obtained from the difference in tip in and tip out results, in Figure 5(b). As can be seen in Figure 5(b), we observed similar peak features corresponding to Cu_2O and CuO. The peak located at 212 cm^{-1} corresponds to Cu_2O, whereas the most intense peak feature at 280 cm^{-1} matches well with the CuO crystals. The peak intensity of Cu_2O was almost the same during the tip in and tip out investigation; however, it shows that the peak intensity signal of CuO is higher during tip in than tip out; thereby indicating that CuO was the surface dominant copper oxide species. This feature is clearly displayed in Figure 5(c), which is the intensity difference between the tip in and tip out measurements. That is, the absence of Cu_2O characteristic peak is indicative of its presence in the bulk rather than on the surface. Thus, taken together the TERS, XPS, and XRD results (measurements made on photoelectrode prepare at 450 ˚C) show that more CuO was present on the surface than in the bulk, which supports our hypothesis that the Cu film on FTO substrate was converted into a thick bottom layer of Cu_2O, with a thin CuO film on the top of Cu_2O.

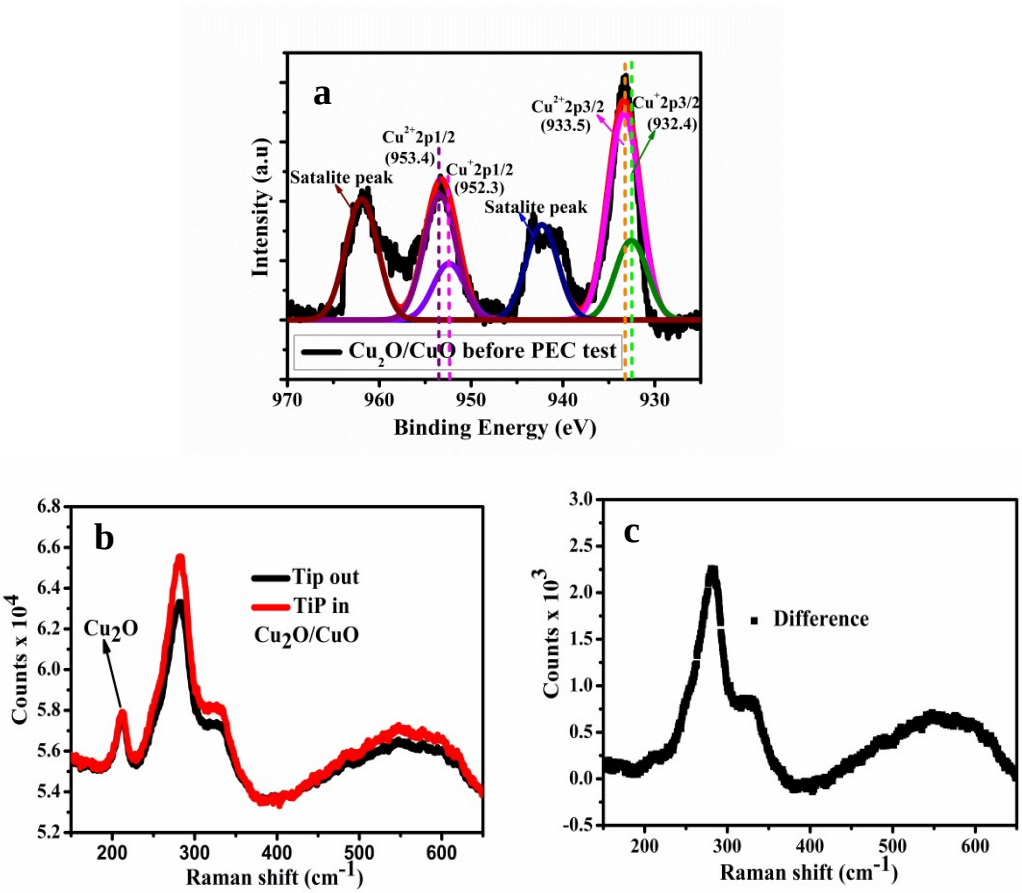

Figure 5. (a) XPS spectra of Cu 2p core level of Cu_2O/CuO (b) TER spectra of Cu_2O/CuO (c) difference curve generated from the TER spectra in Figure 5(b).

Based on the above-mentioned results, we successfully fabricated Cu_2O/CuO heterojunction by this simple and easy approach, and the proposed growth mechanisms of Cu_2O/CuO heterojunction were shown in Scheme 2. During ambient thermal oxidation of the as synthesized Cu film, Cu_2O film is first formed (reaction 3), followed by conversion of parts of Cu_2O to CuO (reaction 4). That is, with the optimum annealing temperature and time, layer-by-layer of Cu_2O and CuO, in which a dense layer of Cu_2O and a thin protective layer of CuO film accompanied with few nanowires on top, are formed.[54] The accepted mechanism for such growth involves outward diffusion of Cu atoms in the Cu film deposited on the FTO substrate and inward diffusion of O atoms during annealing in air.[42] Thus, the reaction between the out diffused Cu atoms from the Cu film on the substrate with oxygen in the air resulted in formation of a Cu_2O layer (reaction 3). The conversion of Cu_2O into CuO results from the diffusion of oxygen into

the films. Cu_2O starts reacting with O and forms the CuO phase according to reaction 4 below. As a result, the FTO substrate was completely covered with a thicker layer of Cu_2O at the bottom and on top of it, a thin protective layer of CuO film. Surface decoration of the Cu_2O/CuO heterojunction (in Scheme 1(c)) will be discussed in a later section.

$$4Cu + O_2 \longrightarrow 2Cu_2O \quad (3)$$

$$1/2Cu_2O + 1/4O_2 \longrightarrow CuO \quad (4)$$

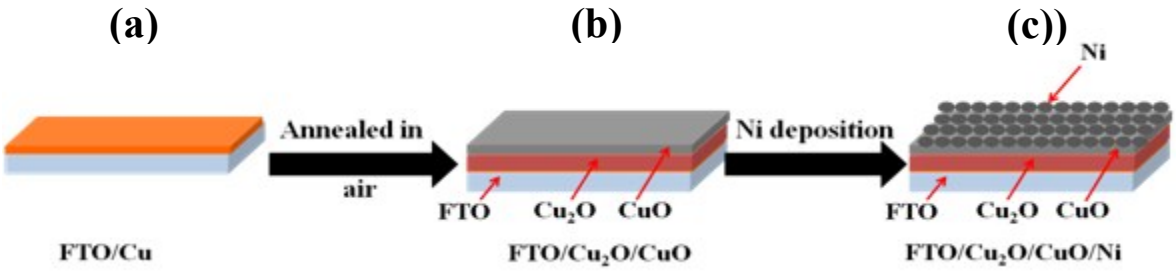

Scheme 2. (a) FTO covered with Cu film (b) thermal oxidation of Cu film on FTO to Cu_2O/CuO heterojunctions and (c) decorating Cu_2O/CuO heterojunctions with Ni.

To understand the effect of Cu_2O/CuO heterojunctions on light absorption, their optical properties were measured with UV–vis diffuse reflectance spectra (DRS). Figure 6 shows the UV–vis absorption spectra of Cu_2O and Cu_2O/CuO heterojunctions prepared at 350, 450, 550 and 650 ˚C, at wavelengths from 350 to 800 nm. An increase in the absorption of light in the short wavelength region (400–600 nm) was observed in all the samples, which can be related to the intrinsic band gap of Cu_2O. As also shown in Figure 6, a similar phenomenon was shown by all the heterojunctions in the long wavelength range (620 to 800 nm). That is, the Cu_2O/CuO heterojunctions, particularly the heterojunction prepared at 450 ˚C, showed a highly enhanced optical absorption in the long wavelength range compared to bare Cu_2O, implying that the incorporation of the heterojunction is able to effectively enhance the solar absorption spectra when compared to a single semiconductor.

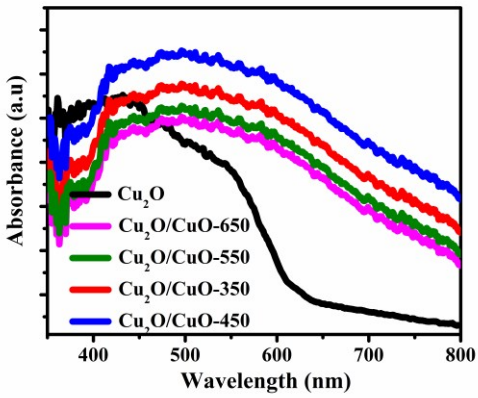

Figure 6 UV–vis diffuse reflectance spectra of Cu film oxidized at 350, 450, 550 and 650 ˚C.

The PEC performance of the Cu_2O/CuO heterojunctions fabricated at different annealing temperatures for 4 hr were also investigated using a conventional three-electrode configuration under chopped AM 1.5 illumination (100 mW/cm^2): Table 1 and Figure S5 show the photoresponse and photostability values dependence on the annealing temperature under these conditions. The results show that the photocurrent density of the Cu_2O/CuO photoelectrodes, fabricated at 450 ˚C, is much higher than that of the photocathodes fabricated at other temperatures. Figure S5b1, shows that the Cu_2O/CuO-450 photocathode gave a photocurrent density of –2.1 mA/cm^2 at 0 V vs. RHE, which is 2, 1.1 and 1.2 times higher than that of a Cu_2O/CuO-350, Cu_2O/CuO-550 and Cu_2O/CuO-650 photocathodes (Figure S5a1, c1 and d1) respectively. The best heterojunction (Cu_2O/CuO-450) yielded a photocurrent density 3.1 times higher than the Cu_2O photocathode (see Table 1) at 0 V vs. RHE. This photocurrent density enhancement is believed to be due to improved crystallinity, synergistic effects and the protective layer of CuO. More interestingly, the Cu_2O/CuO-450 photocathode showed an appreciable enhancement of photocurrent density at higher potentials, indicating the reduction of potential needed by the photoanode in the overall water splitting using the PEC system.

To make the difference more clear, the stability of the photocathodes within 20 minutes of chopped illumination at 0 V vs. RHE was evaluated by comparing the ratio of J/J_o, where J and J_o are the percentages of the photocurrent density at the end of the last light cycle and at the end of the first light cycle respectively.[18] The photocurrent density of Cu_2O/CuO fabricated at 450

˚C (Table 1 and Figure S5b2) at the end of 20 minutes showed a 2.8, 2.2 and 6.5 fold higher photostability (53.6%) compared to the Cu_2O/CuO electrodes fabricated at 350 ˚C (19%), 550 ˚C (24.7% and 650 ˚C (8.3%) respectively (see further information about photostability in the supporting information).

Despite the maximum PEC performance improvement, especially with the Cu_2O/CuO-450 heterojunction having an optimized CuO layer, the stability test still showed photocurrent density decay within 20 minutes (Figure S5b2), indicating CuO alone did not provide sufficient protection for the Cu_2O photocathode. The reason for the observed photocurrent density decay was presumed to be because the CuO Fermi level was not energetic enough for electrons to rapidly transfer to the aqueous electrolyte solution, resulting in the self-reduction of CuO to Cu_2O.

To further improve the photoelectrochemical performance of this system, we examined synergistic effects and cocatalytic surface modification. This is because surface modification with cocatalyst not only effectively promotes water splitting, but also stabilizes the photoelectrode.[55] In photocatalytic systems, it is well known that employing inexpensive, earth abundant cocatalysts e.g. Ni reduces costs, thereby facilitating large scale production. In this study, cocatalytic Ni nanoparticles were used to decorate the Cu_2O/CuO photocathode fabricated at 450 ˚C. Ni nanoparticles prepared by a facile hydrothermal method were dissolved in an alcoholic solution, and deposited on Cu_2O/CuO by spin-coating. The optimum amount of Ni nanoparticles for stable and improved PEC water splitting can be achieved by controlling the number of cycles. Here, the Cu_2O/CuO-450 photocathode decorated with Ni is named as Cu_2O/CuO/Ni-x, where x refers to number of deposition cycle, and the Cu_2O/CuO-450 photocathode is named as bare Cu_2O/CuO or sometimes simply Cu_2O/CuO.

Five Ni modified Cu_2O/CuO photoelectrodes were prepared by repeating the spin-coating deposition cycles with 0.07 M alcoholic solution of nickel nanoparticles. As shown in Figure 7(b), under chopped illumination, the Cu_2O/CuO heterojunction decorated with optimum Ni deposition (Cu_2O/CuO/Ni-3) provided the maximum photocurrent density, –4.3 mA/cm^2 at 0 V vs. RHE, i.e. more than two times higher than the photocurrent density of the undecorated

Cu_2O/CuO photoelectrode (–2.1 mA/cm^2, Figure 7(a)). The promotional effect is more pronounced in the higher potential region than in the lower potential region. Specifically, the photocurrent densities obtained at higher biases for example in the applied potential range of 0.2 –0.4 V vs. RHE are 0.95–0.24 mA/cm^2 and 3.2–1.2 mA/cm^2 for bare Cu_2O/CuO and Cu_2O/CuO/Ni-3 photocathode respectively. This means that the Cu_2O/CuO, decorated with Ni (Cu_2O/CuO/Ni-3), shows a photocurrent increase of ca 330–500% with respect to the undecorated Cu_2O/CuO photocathode. The observed small anodic currents at more positive potentials (from +0.42 V vs. RHE onwards in Figure 7(b)) during light off cycles are presumably due to the oxidation of hydrogen during the illuminated phase of light chopping.[24] It is also noted that the Cu_2O/CuO/Ni-3 photocathode showed a photocurrent onset potential of about 0.61 V vs RHE, which was slightly more positive than the undecorated Cu_2O/CuO (0.55 V vs. RHE) photocathode. The observed shift of the photocurrent onset potential can be attributed to the presence of Ni cocatalyst. This is advantageous in lessening the voltage requirement from the photoanodes and significantly improves the water splitting efficiency. It seems convincing that the enhancement of photocurrent density is due to the synergistic effect of CuO and the incorporated Ni which serves as an efficient cocatalyst for Cu_2O/CuO photocathodes creating a fast transfer of the photogenerated electron from the Cu_2O/CuO surface to the aqueous electrolyte solution, while stabilizing the CuO layer.

Figures 7(c) and (d) show chronoamperometric features related to the photocatalytic stability of the bare Cu_2O/CuO and Cu_2O/CuO/Ni-3 photocathodes under illumination at 0 V vs. RHE in light on/off cycles respectively. As can be seen in Figure 7(c), the bare Cu_2O/CuO showed the maximum photocurrent density (–2.1 mA/cm^2) for the first few seconds with the response gradually decreasing under chopped illumination at 0 V vs. RHE for 20 minutes. However, depositing an optimum layer of Ni on the Cu_2O/CuO photocathode surface (Cu_2O/CuO/Ni-3) revealed a noticeable increase in photocurrent density and photostability (Figure 7(d)). 87.7% initial photocurrent density of Cu_2O/CuO/Ni-3 remains after 20 minutes of standard solar irradiation at 0 V vs. RHE, which is more than 1.5 times compared to the bare Cu_2O/CuO (53.6%), suggesting that surface modification with Ni not only effectively promotes water splitting but also stabilizes the photoelectrode. As shown in Figure S6 and Table 1, the photocurrent density as well as photostability gradually increased as we successively deposited

Ni on Cu_2O/CuO (up to 3 deposition cycles): we found that the Cu_2O/CuO/Ni-3 heterojunction had the highest photocurrent density (–4.3 mA/cm^2) while effectively retaining its photostability. However, the PEC performance of the photocathode decreases when the electrode is decorated beyond 3 cycles of Ni deposition. The observed decrease in photocurrent density was probably due to the blockage of visible light by the Ni layer. As seen in Table 1, the heterostructured Cu_2O/CuO decorated with Ni showed a better PEC performance than the bare or decorated Cu_2O, or the CuO photocathodes, thus demonstrating the potential advantage of fabricating heterostructured Cu_2O/CuO for enhanced light absorption while improving charge carrier transport behavior. Table 1 summarizes the PEC performance using the different photocathodes. The designated photocathode for hydrogen evolution shows remarkable initial photocurrent density of –4.3 mA/cm^{2}at 0 V vs. RHE under AM 1.5 illumination, which is higher than the Cu_2O in the absence of precious coatalysts. The previous works[18, 24] to generate hydrogen from water using Cu_2O photocathode protected with layer by layer deposited inorganic oxides and overcoated with RuO_2 and Pt cocatalysts have shown excellent initial photocurrent density of –5.0 mA/cm^2 and –7.6 mA/cm^2 at 0 V vs. RHE, respectively. The –7.6 mA/cm^2 is the highest value reported in literature. However, the practical application of both systems is severely inflicted by the complexity of the electrodes fabrication as well as the high cost and the scarcity of noble metals. On the contrary, this study demonstrates a comparative performance with Cu_2O/CuO heterostructure decorated by non-precious cocatalyst (Ni) prepared by a facile, scalable, template free, cheap, and environmentally friendly process.

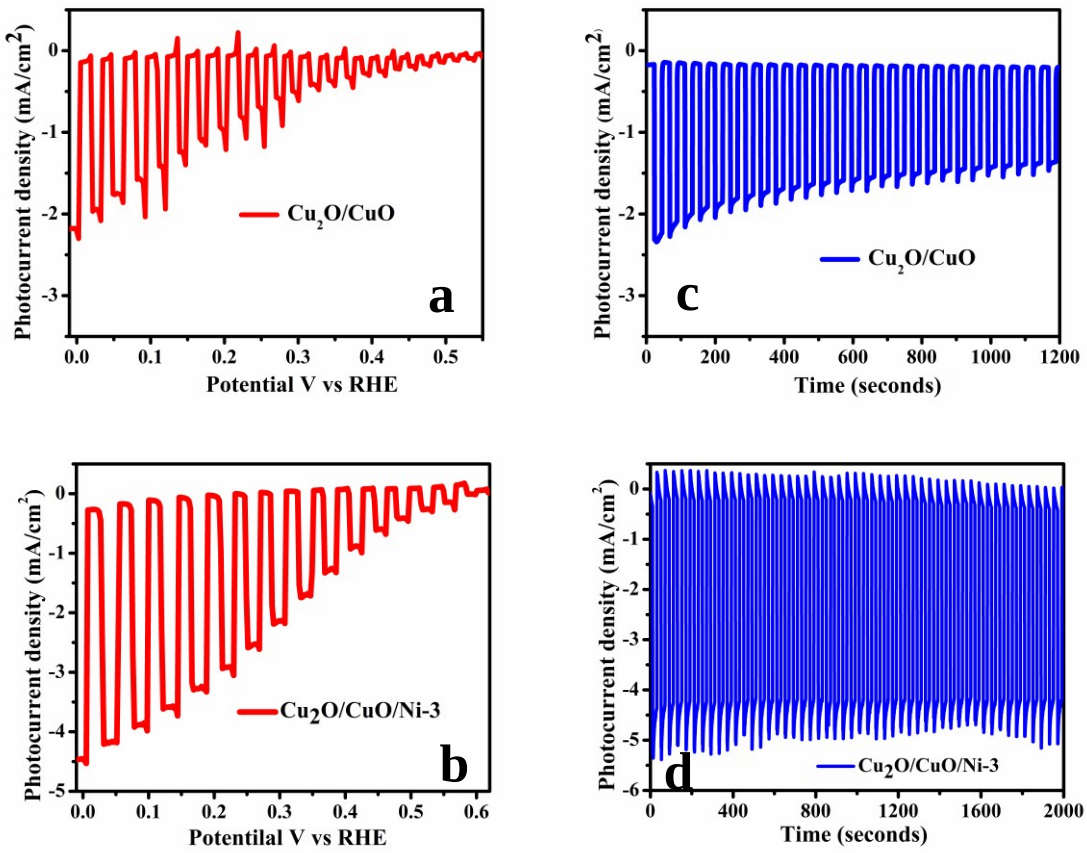

Figure 7. PEC performances and stability measurement of (a and c) Cu_2O/CuO and (b and d) Cu_2O/CuO/Ni-3.

Table 1. Summary of PEC performance for the different photocathodes examined

Sample	Annealing condition	Deposition cycle	Photocurrent density (mA/cm^2)	Stability % (J/J_o) after 20 minutes
Cu_2O/CuO–350	350 ˚C for 4 hr	–	1.1	19.1
Cu_2O/CuO–450	450 ˚C for 4 hr	–	2.1	53.6
Cu_2O/CuO–550	550 ˚C for 4 hr	–	1.9	24.7
Cu_2O/CuO–650	650 ˚C for 4 hr	–	1.8	8.3

Cu_2O/CuO/Ni–1	450 ˚C for 4 hr	1	2.3	63.0
Cu_2O/CuO/Ni–2	450 ˚C for 4 hr	2	3.0	73.3
Cu_2O/CuO/Ni–3	450 ˚C for 4 hr	3	4.3	87.7
Cu_2O/CuO/Ni–4	450 ˚C for 4 hr	4	3.5	74.9
Cu_2O/CuO/Ni–5	450 ˚C for 4 hr	5	1.8	47.7
Cu_2O	350 ˚C for 2 hr	–	0.67	18.0
Cu_2O/Ni–3	350 ˚C for 2 hr	3	0.95	31.2
CuO	650 ˚C for 4 hr	–	1.8	8.3
CuO/Ni–3	650 ˚C for 4 hr	3	2.3	23.4

To confirm whether the generated cathodic photocurrent density is completely due to water reduction, or due to water reduction together with reduction of the photocathode itself (Cu_2O/CuO), we determined the faradaic efficiency of H_2 production for each photocathode. To evaluate the faradaic efficiency of the photocathodes, the generated H_2 was quantified using a gas chromatograph and the corresponding charge, Q_{H2}, was compared to the total charge, Q_{tot}, obtained by integration of the photocurrent density (Figure S7a), measured at 0 V vs. RHE under AM 1.5 illumination. After passing 2.7 C (Figure S7a) through the Cu_2O/CuO/Ni-3 photocathode at 0 V vs. RHE under AM 1.5 illumination, 0.0118 mmole H_2 was detected, corresponding to a faradic efficiency of 84%. This faradic efficiency is lower than unit, revealing that the current due to photocatalytic hydrogen evolution might include a contribution from the reduction of the protective layer, i.e. CuO, to Cu_2O. However, detailed characterization (SEM, XRD, XPS and XANES in the next section) of the photocathode after photoelectrochemical tests for 20 minutes at 0 V vs. RHE under AM 1.5 illumination reveals almost no corrosion of the electrode. Thus, the H_2 evolution efficiency was less than 100%, possibly due to unwanted

backward reactions between H_2 and O_2,[56] or dissolution in the electrolyte solution.[57] We also determined the faradaic efficiency of a bare Cu_2O/CuO photocathode under the same conditions: the bare Cu_2O/CuO photocathode evolved four orders less H_2, i.e. 0.0035 mmole, after passing 1.2 C, equivalent to a faradaic efficiency of 57%; thereby indicating that the photoreduction of the protective layer is more serious with bare photocathodes. In spite of these limitations, the present study shows that the Cu_2O/CuO photocathode decorated with nickel has a better PEC performance with suppression of photocorrosion property compared to the bare Cu_2O/CuO photocathode.

To quantitatively evaluate the efficiency of PEC water splitting in terms of applied bias photon-to-current efficiency (ABPE), photocurrent density versus applied potential (J-V) curves of Cu_2O/CuO and Cu_2O/CuO/Ni-3 photocathodes were measured in a two electrode configuration in the dark and under simulated one sun illumination (Figure S7b). The features of observed linear sweep voltammetry curves, measured in two electrode systems, were similar to LSV curves measured in three electrode systems shown in Figure 7. The photoconversion efficiency (ABPE) is calculated using equation 5:[58, 59]

$$\mathrm{ABPE} = \left[\frac{|J_{ph}|(\mathrm{mA/cm^2}) \times (1.23 - |V_b|)(\mathrm{V})}{P_{total(\mathrm{mW/cm^2})}}\right]_{\mathrm{AM\ 1.5G}}, \qquad (5)$$

where j_{ph} is the photocurrent density obtained under an applied bias V_b between the working and the counter electrodes, 1.23 V is the standard water splitting reaction potential and P_{total} is the incident light intensity (which is 100 mW/cm^2). As shown in Figure S7b, the photocatalytic activity of the bare Cu_2O/CuO and Cu_2O/CuO/Ni-3 photocathodes was almost negligible when the bias was zero and under dark conditions using a potential scan from 0.10 V to –0.61 V vs. Pt electrode. This indicates that little hydrogen was generated in the absence of solar energy; however, under simulated one sun illumination an enhanced cathodic photocurrent density was observed over the entire potential range, confirming the capability of the photocathode to produce hydrogen. Looking into a potential region for example at –0.4 V and at –0.3 V vs. Pt electrode, the bare Cu_2O/CuO photocathode revealed conversion efficiencies of 0.58% and 0.53% respectively. More interestingly, the Cu_2O/CuO/Ni-3 photocathode revealed corresponding

conversion efficiencies of 2.71% and 2.0 % at the same applied bias (–0.4 V and –0.3 V) – indicating a greater than 460% and 370% increase in efficiency with respect to the Cu_2O/CuO photocathode. These improvements are attributed to efficient surface charge transfer by Cu_2O/CuO/Ni-3, which has the maximum photocurrent densities at more positive potentials. Surface modification of Cu_2O/CuO by Ni promotes the transfer of photoinduced charge carriers (electrons) from the Cu_2O/CuO surface to the aqueous solution, resulting in a facilitated hydrogen evolution reaction by lowering the hydrogen evolution reaction overpotential. Increased maximum photocurrent density and an anodic shift in onset potential significantly enhanced the photoconversion efficiency of the Cu_2O/CuO/Ni-3 photocathode.

To understand the electron transfer activity at the photocathodes/solution interface, we compared electrochemical impedance spectra (EIS) of a photocathode decorated with Ni nanoparticles (Cu_2O/CuO/Ni-3) and a bare photocathode (Cu_2O/CuO) under simulated one sun illumination and dark conditions (Figure 8) at a potential of 0 V vs. RHE. The semicircular feature of the Nyquist plots (Figure 8) at high frequencies is the defining characteristic of the charge transfer process where the diameter of the semicircle is equal to the charge transfer resistance (R_{ct}).[26] As shown in Figure 8, the appearance of semicircular features of EIS measurement both in dark and under illumination was observed, suggesting charge transfer resistance controlling the kinetics at the electrode interface.[60, 61] For both electrodes (Cu_2O/CuO and Cu_2O/CuO/Ni-3), the arc radii under illumination were much smaller than that in the dark, which is due to the increased electron conductivity of the electrodes when irradiated. The incorporation of Ni as co-catalyst (Cu_2O/CuO/Ni-3) caused a significant decrease in the radius of the arc compared with bare Cu_2O/CuO under irradiation, suggesting that the deposition of Ni on the Cu_2O/CuO surface facilitates the transfer of photo-induced electrons from the Cu_2O/CuO surface to the electrolyte solution.

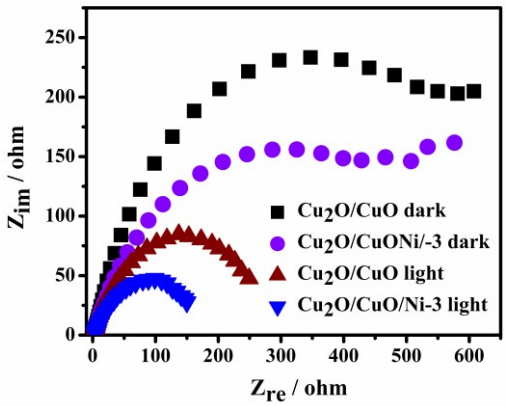

Figure 8. Nyquist plots of Cu_2O/CuO and Cu_2O/CuO/Ni-3 based photocathodes both in dark and under AM 1.5 illumination in 1.0 M Na_2SO_4 electrolyte buffered at pH 5.0.

We also used SEM, XRD, XPS and XANES to characterize the composition of the photocathodes after photoelectrochemical test for 20 minutes at 0 V vs. RHE under AM 1.5 illumination. Figure 9 compares the morphology of bare Cu_2O/CuO and Cu_2O/CuO/Ni-3 before and after the stability test. After 20 minutes illumination the morphology of the Cu_2O/CuO/Ni-3 (Figure 9(b)) did not change significantly. A slightly changed distribution of nickel nanoparticles in some areas was observed after 20 minutes, probably due to detached outermost nickel cocatalyst being incorporated into the electrolyte solution. However, as can be seen from the SEM image in Figure 9(d), the bare Cu_2O/CuO electrode experienced a significant surface change resulting from the formation of a black sheet like film over the inner film, possibly due to corrosion of the outer CuO layer that directly contacts with the electrolyte solution.

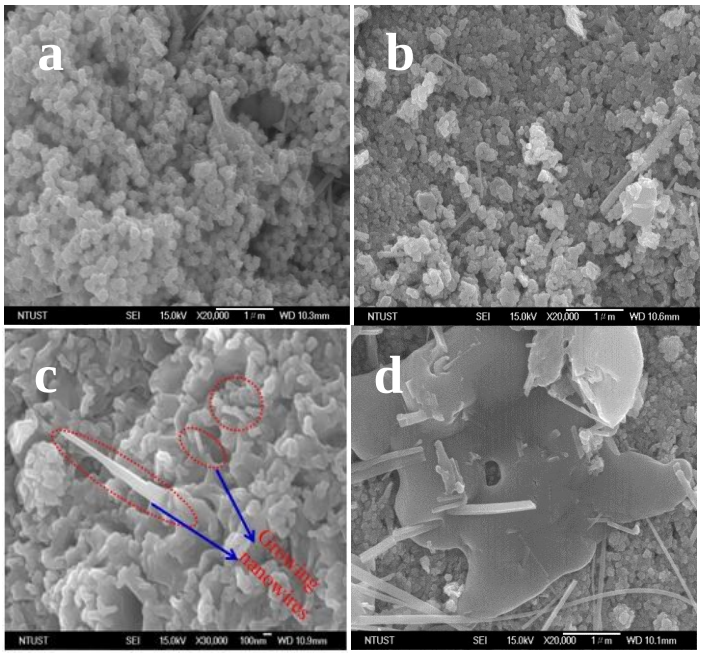

Figure 9. FE SEM images of (a) Cu_2O/CuO/Ni-3 before the PEC test; (b) Cu_2O/CuO/Ni-3 after the PEC test; (c) Cu_2O/CuO before the PEC test and (d) Cu_2O/CuO after PEC test for 20 minutes.

Similarly, we also carried out XPS measurements of the Cu_2O/CuO/Ni-3 and Cu_2O/CuO photocathodes after stability testing. Compared with the XPS results in Figure 5 (before PEC test), the XPS result obtained from the Cu_2O/CuO/Ni-3 photocathode (Figure 10(a)) after the stability test, i.e. 20 mins illumination at 0 V vs. versus RHE, showed the presence of binding energy peaks related to Cu 2p3/2 and Cu 2p1/2 of Cu_2O and CuO, thereby indicating the preservation of the protecting layer CuO. However, the Cu 2p XPS spectrum of the Cu_2O/CuO photocathode after stability test in Figure 10(b) revealed the absence of Cu 2p3/2 and Cu 2p1/2 peaks, thereby indicating corrosion of the CuO protecting layer. Similar information was also obtained from XRD data (Figures S8a and b), demonstrating that the deposition of Ni on Cu_2O/CuO not only enhanced the photocurrent density for the hydrogen evolution reaction but also appreciably preserved the photocatalytic stability of the CuO protective layer. Further information about nickel deposition is presented in the supporting information.

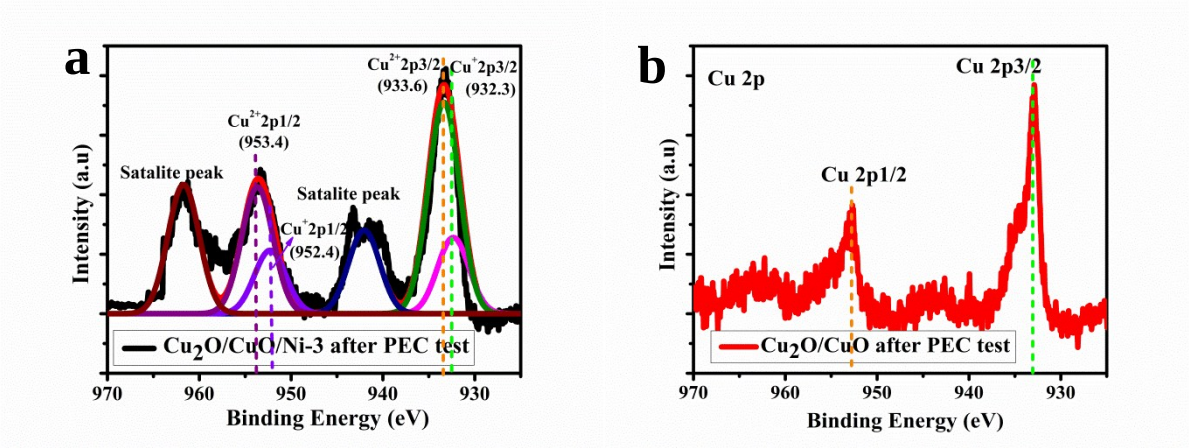

Figure 10. XPS spectra of: (a) Cu 2p core level of Cu_2O/CuO/Ni-3 after PEC test and (b) Cu 2p core level of Cu_2O/CuO after PEC test.

To investigate the chemical composition of the photocathodes, XANES and EXAFS were taken for Cu_2O/CuO and Cu_2O/CuO/Ni-3 samples both before and after the PEC test, see Figure 11(a). The enlarged portion of the area (in Figure 11(a)) from 8977 to 8989 eV is shown in Figure 11(b), which reveals that the XANES spectra of Cu_2O/CuO and Cu_2O/CuO/Ni before the PEC test are almost the same. However, after the PEC test the edge position of Cu_2O/CuO is shifted 0.8 eV to a lower position, indicating the average oxidation state of Cu species is reduced: this reduction was found to be significantly suppressed after incorporating nickel. The nickel decorated photocathode (Cu_2O/CuO/Ni-3) showed a relatively smaller shift in edge position (0.3 eV) after the PEC test (in the direction shown in Figure 11(b)), indicating the better stability of the heterojunction. This is in good agreement with our XRD and XPS data. We further checked the Ni K-edge XANES (Figures S11a and b) and found that the oxidation state of Ni is also slightly reduced after PEC measurement, indicating that the Ni can protect the CuO to maintain the heterojunction (see further information in the supporting information).

In agreement with the XANES spectra, the Fourier transform magnitudes or κ^2- weighted Cu-*K*-edge EXAFS spectra (shown in Figure 11(c), (d)) of Cu_2O/CuO/Ni-3 both before and after the PEC test are similar with two main peaks below 3.5 Å. A broad intense peak at 2.4 Å (Figure 11(c)) matches well with Cu–Cu bonds, whereas the second peak centered at about 1.6 Å is due to the Cu–O bonds of Cu_2O, consistent with our previous reports.[25] As seen Figure 11(c), the

nickel decorated Cu_2O/CuO photocathode (Cu_2O/CuO/Ni-3) showed stable structure feature after the PEC test, however the intensity of the Cu–Cu bond in Cu_2O/CuO after the PEC test increases significantly compared to its initial state, indicating an increase in the crystalline size of Cu_2O, probably due to the reduction of the CuO layer. A similar feature is observed in Figure 11(d), i.e. after the PEC test, the oscillation change is significant in bare Cu_2O/CuO (blue curve in Figure 11(d)) indicating a bigger crystal size; however only a slight change was observed in nickel modified Cu_2O/CuO, confirming its greater stability compared to bare Cu_2O/CuO. The results displayed here are consistent with the XRD results.

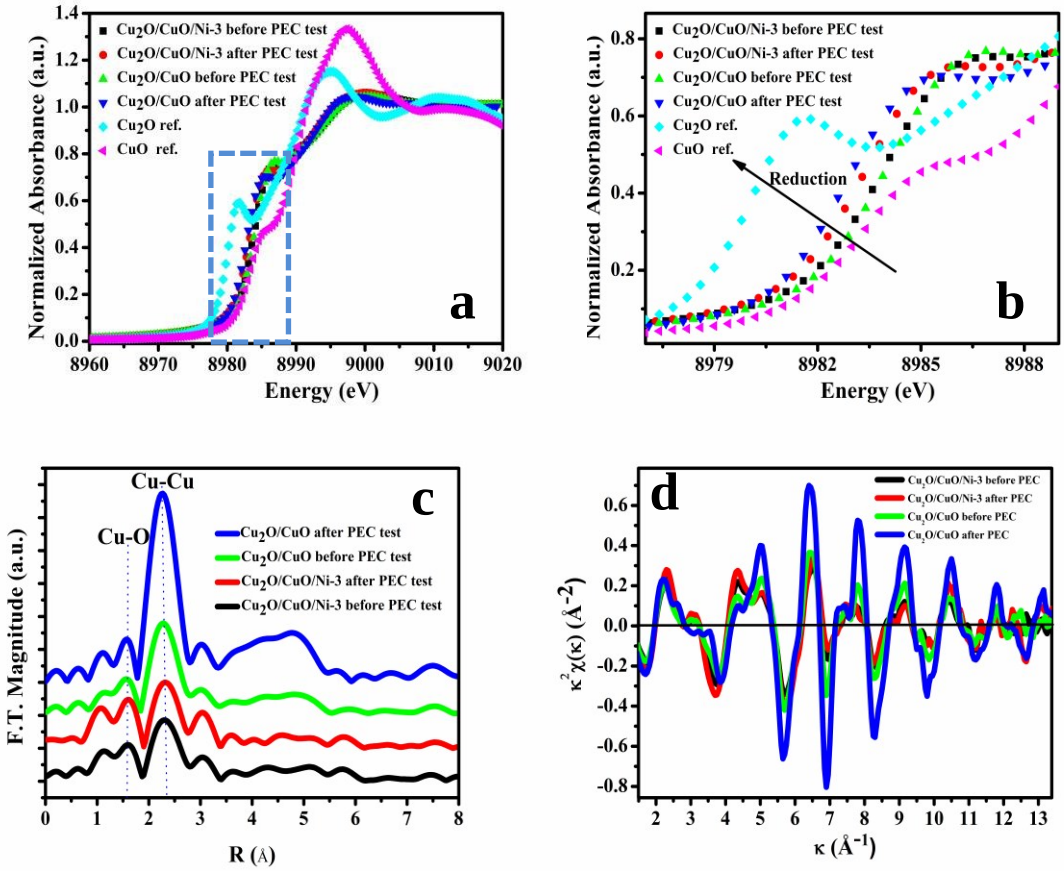

Figure 11. (a) Cu-K-edge XANES spectra of Cu_2O/CuO and Cu_2O/CuO/Ni-3 both before and after PEC; (b) enlargement of selected portion of curve a and (c, d) Cu-K-edge EXAFS spectra of Cu_2O/CuO and Cu_2O/CuO/Ni-3 both before and after PEC in r and κ- space respective.

Band alignment and charge transfer between Cu_2O and CuO, were studied using Tauc and Mott–Schottky (MS) plot studies on pure Cu_2O and CuO samples. Figure S14(a) shows the Tauc plots of pure Cu_2O and CuO, obtained from UV-vis spectra based on Tauc equation, which reveal band gaps of 2.01 and 1.54 eV for Cu_2O and CuO respectively. These values are in good agreement with existing literature reports.[49] Thus, to illustrate the band alignments of Cu_2O and CuO together with Tauc plots, we determined the flat band potential and hole concentration (N_A) of pure Cu_2O and pure CuO by performing Mott−Schottky measurements. The Mott−Schottky plot relates the inverse of the square capacitance with potential at a fixed frequency of 1 kHz, see equation below:

$$\frac{1}{C^2} = \frac{2}{\varepsilon_o \varepsilon e N_A A^2}\left(\mathrm{V} - V_{fb} - \frac{k_B T}{e}\right) \quad (6)$$

where C and ε_o are the space-charge capacitance of the semiconductor and the permittivity in vacuum respectively, ε is the dielectric constant of Cu_2O (taken as 7.6)[62] and CuO (taken as 10.26),[31] e is the electronic charge, V_{fb} is the flat-band potential, V is the applied potential, N_A is the number density of acceptors in Cu_2O or CuO, T is the absolute temperature, A is area of the electrode and k_B is the Boltzmann constant. The flat band potential (V_{fb}) is determined (using equation 7 below) after the small thermal correction (k_BT/e) of the intercept (V_o)[63] which is estimated from extrapolating the linear part of the curve to $1/C^2$ equal to zero on the potential axis.

$$V_{fb} = V_o + {}^{k_B T}/_{e} \quad (7)$$

The carrier density (N_A), was calculated from the slopes of the Mott-Schottky plots:

$$N_A = {}^{2}/_{\varepsilon \varepsilon_o S e A^2} \quad (8)$$

Figure S14(b) and (c) show the Mott−Schottky plots for the Cu_2O and CuO in 1.0 M Na_2SO_4 electrolyte (pH 5). Figures S14(b) and (c), show that besides the p-type behavior (negative slopes of $1/C^2$ vs potential linear plots), the Mott−Schottky measurement gives the flat-band potential of 0.63 and 0.74 V vs. RHE for Cu_2O and CuO respectively, while the hole concentration of N_A for

Cu_2O and CuO was 3.4 x 10^{17} cm^{-3} and 4.1 x10^{18} cm^{-3} respectively. More than ten times increase in doping concentration (N_A) in CuO, resulted in a reduced charge depletion layer, implying incorporation of the CuO layer in the Cu_2O/CuO heterojunction played a role in suppressing electron/hole recombination within the charge depletion region.[32] Since the flatband potentials could be taken as a reasonable approximation to the valence band (VB) edges (≤ 100 mV) for the p-type conductors[44–46], one can evaluate the conduction band edge position by using the respective optical bandgaps of Cu_2O and CuO.

Based on the above results, a possible PEC water splitting mechanism is proposed in Scheme 3. The relatively poor photocurrent density and photostability of the Cu_2O film was ascribed to poor crystallinity and slow charge carrier transfer. Compared to Cu_2O, the Cu_2O/CuO heterojunction shows not only enhanced photocurrent density but also improved photostability, due to enhanced crystallinity and synergistic effects. Due to their appropriate band alignment, the photogenerated electrons on Cu_2O, transfer to the conduction band of CuO and the hole from CuO transfers to the valence band of Cu_2O. Therefore, the Cu_2O/CuO hetrojenction enhances the light harvesting and charge separation efficiency (noted as medium transfer), resulting in an improved PEC water splitting performance. Further improvements in photocurrent density and photostability were made by decorating the Cu_2O/CuO photocathode with nickel, resulting in the fast transfer of photoinduced charge carriers (electrons) from the Cu_2O/CuO surface to the aqueous solution and surface stabilization. This is probably because, Ni has no band gap and exhibits a high electrocatalytic activity [44] that guarantees a very low HER overpotential on Ni. Moreover, Ni has greater tendency to shift its Fermi level to a more negative potential close to the CB level of CuO, due to the transfer of electrons into the Ni cocatalyst.[64] As a result, accumulated electrons on metal particles can be transferred to protons adsorbed on the surface to further reduce the protons to hydrogen molecules, while the migrated photo-generated holes at the valence band of CuO to valence band of Cu_2O will be transported to the counter electrode (anode) to facilitate oxygen evolution. Thus, the photogenerated electron−hole pairs are effectively separated, which is crucial for the enhancement of PEC activity. We believe that the synergistic effects induced by forming Cu_2O/CuO heterojunction and incorporation of Ni cocatalyst greatly accelerate electron transfer and effectively retard the reduction of CuO by photo-generated electrons.

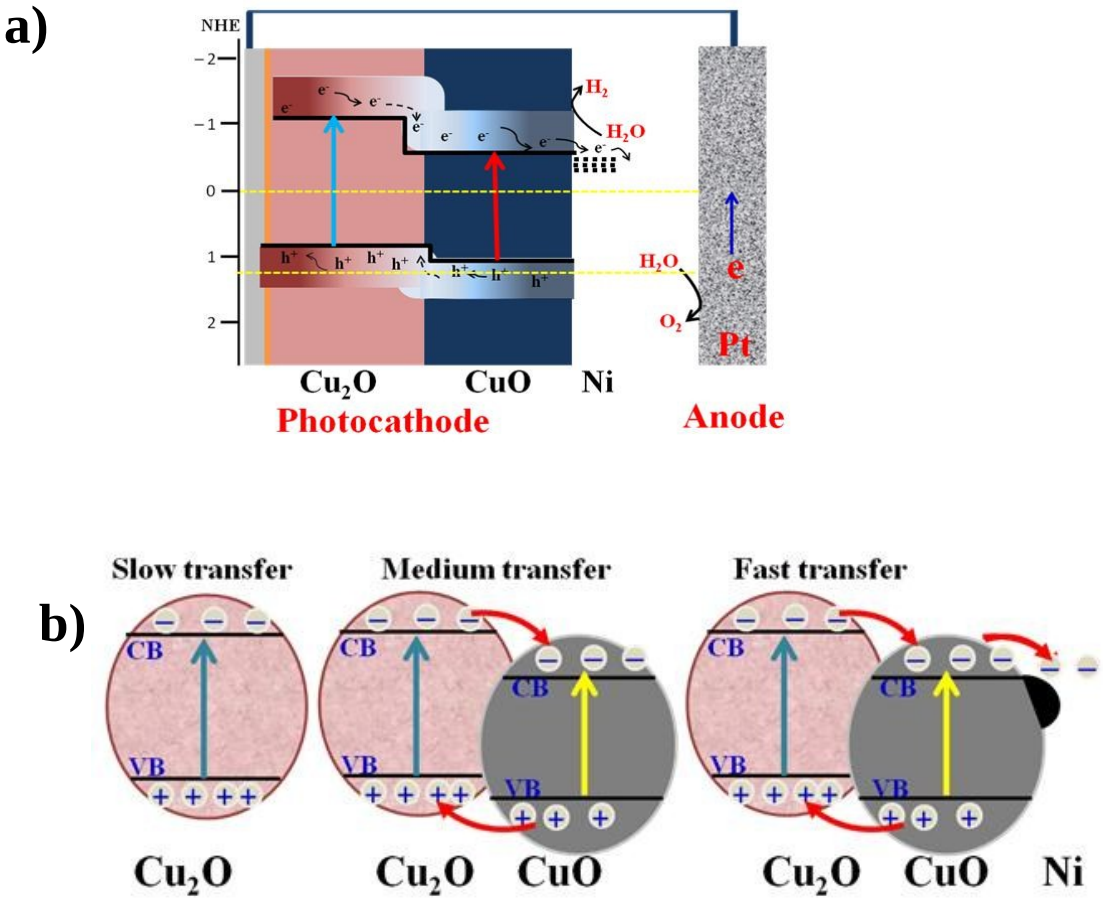

Scheme 3. (a) Proposed mechanism of PEC water splitting and (b) the energy band structure of Cu_2O, Cu_2O/CuO and Cu_2O/CuO/Ni.

Conclusions

In summary, we have developed a highly efficient and promising Cu_2O/CuO photocathode decorated with nickel for water reduction using a simple, inexpensive and facile method, comprising electrolysis deposition, thermal annealing in air and spin-coating processes. The highest photocurrent density and stability (–2.1 mA/cm^2 and 53% respectively) was recorded using a bare Cu_2O/CuO heterojunction fabricated at 450 ˚C for 4 hour, due to its improved crystalline quality and the synergistic effects conferred by the CuO layer. The photocurrent density improved to –4.3 mA/cm^2 at 0 V vs. RHE when using the Cu_2O/CuO heterojunction decorated with Ni cocatalyst. The Cu_2O/CuO photocathode decorated with nickel maintained ~ 87.7% of the initial photocurrent density after 20 minutes illumination at 0 V vs. RHE, giving the best resistance to photocorrosion when compared to the bare Cu_2O/CuO photocathode under the same condition. More intriguingly, the Cu_2O/CuO photocathode decorated with nickel reached a maximum solar conversion efficiency of 2.71% at an applied potential of –0.4 V vs. Pt which accounts to a greater than 460% efficiency improvement with respect to the bare Cu_2O/CuO (0.58%) at the same applied bias. To the best of our knowledge, this is first and best report of stability, photocurrent density and solar energy conversion efficiency obtained by a Cu_2O/CuO photocathode decorated with Ni in PEC water splitting. As evidenced by XRD, SEM, XPS, XAS and EXAFS, the improved PEC performance is attributed to preservation of the protective layer against photocorrosion, due to surface activation of the heterostructured Cu_2O/CuO with nickel nanoparticles. The work in this study reveals a promising strategy for inhibiting photocorrosion problems associated with unstable semiconductors by incorporating an optimum protective layer and a surface decorated with cocatalyst.

Acknowledgments

The financial supports from the Ministry of Science and Technology (MoST)(103-3113-E-011 - 001, 101-3113-E-011-002, 101-2923-E-011-001-MY3, 100-2221-E-011-105-MY3), and the Top University Projects of Ministry of Education (MOE) (100H451401), as well as the facilities supports from the National Synchrotron Radiation Research Center (NSRRC) and National Taiwan University of Science and Technology (NTUST) are acknowledged.

References

1. D. Gust, T. A. Moore and A. L. Moore,Mimicking Photosynthetic Solar Energy Transductions *Acc. Chem. Res.*, 2000, **34**, 40-48.
2. E. Ochoa-Fernández, H. K. Rusten, H. A. Jakobsen, M. Rønning, A. Holmen and D. Chen,Sorption enhanced hydrogen production by steam methane reforming using Li_2ZrO_3 as sorbent: Sorption kinetics and reactor simulations *Catal. Today*, 2005, **106**, 41-46.
3. D. Yu, M. Aihara and M. J. Antal,Hydrogen production by steam reforming glucose in supercritical waters *Energy & Fuels*, 1993, **7**, 574-577.
4. B. Zhang, X. Tang, Y. Li, Y. Xu and W. Shen,Hydrogen production from steam reforming of ethanol and glycerol over ceria-supported metal catalystss *Int. J. Hydrogen Energy*, 2007, **32**, 2367-2373.
5. J. Nowotny, C. C. Sorrell, L. R. Sheppard and T. Bak,Solar-hydrogen: Environmentally safe fuel for the futures *Int. J. Hydrogen Energy*, 2005, **30**, 521-544.
6. X. Lu, S. Xie, H. Yang, Y. Tong and H. Ji,Photoelectrochemical hydrogen production from biomass derivatives and waters *Chem. Soc. Rev.*, 2014, **43**, 7581--7593.
7. S. Czernik, R. Evans and R. French,Hydrogen from biomass-production by steam reforming of biomass pyrolysis oils *Catal. Today*, 2007, **129**, 265-268.
8. M. Ni, D. Y. C. Leung, M. K. H. Leung and K. Sumathy,An overview of hydrogen production from biomasss *Fuel Process. Technol.*, 2006, **87**, 461-472.
9. M. Moriya, T. Minegishi, H. Kumagai, M. Katayama, J. Kubota and K. Domen,Stable Hydrogen Evolution from CdS-Modified $CuGaSe_2$ Photoelectrode under Visible-Light Irradiations *J. Am. Chem. Soc.*, 2013, **135**, 3733-3735.
10. M. H. Lee, K. Takei, J. Zhang, R. Kapadia, M. Zheng, Y.-Z. Chen, J. Nah, T. S. Matthews, Y.-L. Chueh, J. W. Ager and A. Javey,p-Type InP Nanopillar Photocathodes for Efficient Solar-Driven Hydrogen Productions *Angew. Chem. Int. Ed.*, 2012, **51**, 10760-10764.
11. C. Liu, J. Sun, J. Tang and P. Yang,Zn-Doped p-Type Gallium Phosphide Nanowire Photocathodes from a Surfactant-Free Solution Synthesiss *Nano Lett.*, 2012, **12**, 5407-5411.
12. Y. Hou, B. L. Abrams, P. C. K. Vesborg, M. E. Björketun, K. Herbst, L. Bech, A. M. Setti, C. D. Damsgaard, T. Pedersen, O. Hansen, J. Rossmeisl, S. Dahl, J. K. Nørskov and I. Chorkendorff,Bioinspired molecular co-catalysts bonded to a silicon photocathode for solar hydrogen evolutions *Nat. Mater.*, 2011, **10**, 434-438.
13. Y. Lin, C. Battaglia, M. Boccard, M. Hettick, Z. Yu, C. Ballif, J. W. Ager and A. Javey,Amorphous Si Thin Film Based Photocathodes with High Photovoltage for Efficient Hydrogen Productions *Nano Lett.*, 2013, **13**, 5615-5618.
14. X. Mathew, A. Bansal, J. A. Turner, R. Dhere, N. R. Mathews and P. J. Sebastian,Photoelectrochemical Characterization of Surface Modified CdTe for Hydrogen Productions *J. New Mater. Electrochem. Syst.*, 2002, **5**, 149-154.
15. J. R. McKone, A. P. Pieterick, H. B. Gray and N. S. Lewis,Hydrogen Evolution from Pt/Ru-Coated p-Type WSe_2 Photocathodess *J. Am. Chem. Soc.*, 2012, **135**, 223-231.
16. A. Paracchino, N. Mathews, T. Hisatomi, M. Stefik, S. D. Tilley and M. Gratzel,Ultrathin films on copper(i) oxide water splitting photocathodes: a study on performance and stabilitys *Energy Environ. Sci*, 2012, **5**, 8673-8681.

17. C. G. Morales-Guio, S. D. Tilley, H. Vrubel, M. Gratzel and X. Hu,Hydrogen evolution from a copper(I) oxide photocathode coated with an amorphous molybdenum sulphide catalysts *Nat. Commun.*, 2014, **5**, 3059.
18. A. Paracchino, V. Laporte, K. Sivula, M. Grätzel and E. Thimsen,Highly active oxide photocathode for photoelectrochemical water reductions *Nat. Mater.*, 2011, **10**, 456-461.
19. L. Hu, Y. Huang, F. Zhang and Q. Chen,CuO/Cu_2O composite hollow polyhedrons fabricated from metal-organic framework templates for lithium-ion battery anodes with a long cycling lifes *Nanoscale*, 2013, **5**, 4186-4190.
20. M. Hasan, T. Chowdhury and J. F. Rohan,Nanotubes of Core/Shell Cu / Cu_2O as Anode Materials for Li-Ion Rechargeable Batteriess *J. Electrochem. Soc.*, 2010, **157**, A682-A688.
21. W.-C. Huang, L.-M. Lyu, Y.-C. Yang and M. H. Huang,Synthesis of Cu_2O Nanocrystals from Cubic to Rhombic Dodecahedral Structures and Their Comparative Photocatalytic Activitys *J. Am. Chem. Soc.*, 2011, **134**, 1261-1267.
22. M. Wang, L. Sun, Z. Lin, J. Cai, K. Xie and C. Lin,p-n Heterojunction photoelectrodes composed of Cu_2O-loaded TiO_2 nanotube arrays with enhanced photoelectrochemical and photoelectrocatalytic activitiess *Energy Environ. Sci*, 2013, **6**, 1211-1220.
23. Y.-F. Zhao, Z.-Y. Yang, Y.-X. Zhang, L. Jing, X. Guo, Z. Ke, P. Hu, G. Wang, Y.-M. Yan and K.-N. Sun,Cu_2O Decorated with Cocatalyst MoS_2 for Solar Hydrogen Production with Enhanced Efficiency under Visible Lights *J. Phys. Chem. C*, 2014, **118**, 14238-14245.
24. S. D. Tilley, M. Schreier, J. Azevedo, M. Stefik and M. Graetzel,Ruthenium Oxide Hydrogen Evolution Catalysis on Composite Cuprous Oxide Water-Splitting Photocathodess *Adv. Funct. Mater.*, 2014, **24**, 303-311.
25. A. A. Dubale, W.-N. Su, A. G. Tamirat, C.-J. Pan, B. A. Aragaw, H.-M. Chen, C.-H. Chen and B.-J. Hwang,The synergetic effect of graphene on Cu_2O nanowire arrays as a highly efficient hydrogen evolution photocathode in water splittings *J. Mater. Chem. A*, 2014, **2**, 18383-18397.
26. Z. Zhang, R. Dua, L. Zhang, H. Zhu, H. Zhang and P. Wang,Carbon-Layer-Protected Cuprous Oxide Nanowire Arrays for Efficient Water Reductions *ACS Nano*, 2013, **7**, 1709-1717.
27. C.-Y. Lin, Y.-H. Lai, D. Mersch and E. Reisner,$Cu_2O|NiO_x$ nanocomposite as an inexpensive photocathode in photoelectrochemical water splittings *Chem. Sci.*, 2012, **3**, 3482-3487.
28. X. Guo, P. Diao, D. Xu, S. Huang, Y. Yang, T. Jin, Q. Wu, M. Xiang and M. Zhang,CuO/Pd composite photocathodes for photoelectrochemical hydrogen evolution reactions *Int. J. Hydrogen Energy*, 2014, **39**, 7686-7696.
29. Z. Liu, H. Bai, S. Xu and D. D. Sun,Hierarchical CuO/ZnO "corn-like" architecture for photocatalytic hydrogen generations *Int. J. Hydrogen Energy*, 2011, **36**, 13473-13480.
30. X. Zhao, P. Wang and B. Li,CuO/ZnO core/shell heterostructure nanowire arrays: synthesis, optical property, and energy applications *Chem. Commun.*, 2010, **46**, 6768-6770.
31. Z. Zhang and P. Wang,Highly stable copper oxide composite as an effective photocathode for water splitting via a facile electrochemical synthesis strategys *J. Mater. Chem.*, 2012, **22**, 2456-2464.

32. Q. Huang, F. Kang, H. Liu, Q. Li and X. Xiao,Highly aligned $Cu_2O/CuO/TiO_2$ core/shell nanowire arrays as photocathodes for water photoelectrolysiss *J. Mater. Chem. A*, 2013, **1**, 2418-2425.
33. S. Eisermann, A. Kronenberger, A. Laufer, J. Bieber, G. Haas, S. Lautenschläger, G. Homm, P. J. Klar and B. K. Meyer,Copper oxide thin films by chemical vapor deposition: Synthesis, characterization and electrical propertiess *Phys. Status Solidi A*, 2012, **209**, 531-536.
34. E. Comini, G. Sberveglieri, D. Barreca, C. Sada, A. Gasparotto, C. Maccato and E. Tondello,Chemical Vapor Deposition of Cu_2O and CuO nanosystems for innovative gas sensorss *Ieee Sensors. Proceedings*, 2009, 111-113.
35. D. Barreca, P. Fornasiero, A. Gasparotto, V. Gombac, C. Maccato, T. Montini and E. Tondello,The Potential of Supported Cu_2O and CuO Nanosystems in Photocatalytic H_2 Productions *ChemSusChem*, 2009, **2**, 230-233.
36. J.-N. Nian, C.-C. Hu and H. Teng,Electrodeposited p-type Cu_2O for H_2 evolution from photoelectrolysis of water under visible light illuminations *Int. J. Hydrogen Energy*, 2008, **33**, 2897-2903.
37. R. P. Wijesundera,Fabrication of the $CuO-Cu_2O$ heterojunction using an electrodeposition technique for solar cell applicationss *Semicond. Sci. Technol.*, 2010, **25**, 045015.
38. W.-Y. Yang, W.-G. Kim and S.-W. Rhee,Radio frequency sputter deposition of single phase cuprous oxide using Cu_2O as a target material and its resistive switching propertiess *Thin Solid Films*, 2008, **517**, 967-971.
39. Q. Simon, D. Barreca, A. Gasparotto, C. Maccato, T. Montini, V. Gombac, P. Fornasiero, O. I. Lebedev, S. Turner and G. Van Tendeloo,Vertically oriented CuO/ZnO nanorod arrays: from plasma-assisted synthesis to photocatalytic H_2 productions *J. Mater. Chem.*, 2012, **22**, 11739-11747.
40. Y.-k. Su, C.-m. Shen, H.-t. Yang, H.-l. Li and H.-j. Gao,Controlled synthesis of highly ordered CuO nanowire arrays by template-based sol-gel routes *Trans. Nonferrous Met. Soc. China*, 2007, **17**, 783-786.
41. F. Teng, W. Yao, Y. Zheng, Y. Ma, Y. Teng, T. Xu, S. Liang and Y. Zhu,Synthesis of flower-like CuO nanostructures as a sensitive sensor for catalysiss *Sensors and Actuators B: Chemical*, 2008, **134**, 761-768.
42. P. Wang, Y. H. Ng and R. Amal,Embedment of anodized p-type Cu_2O thin films with CuO nanowires for improvement in photoelectrochemical stabilitys *Nanoscale*, 2013, **5**, 2952-2958.
43. S. P. Berglund, H. He, W. D. Chemelewski, H. Celio, A. Dolocan and C. B. Mullins,p-Si/W_2C and p-Si/W_2C/Pt Photocathodes for the Hydrogen Evolution Reactions *J. Am. Chem. Soc.*, 2014, **136**, 1535-1544.
44. A. K. Agegnehu, C.-J. Pan, J. Rick, J.-F. Lee, W.-N. Su and B.-J. Hwang,Enhanced hydrogen generation by cocatalytic Ni and NiO nanoparticles loaded on graphene oxide sheetss *J. Mater. Chem.*, 2012, **22**, 13849-13854.
45. J. R. McKone, E. L. Warren, M. J. Bierman, S. W. Boettcher, B. S. Brunschwig, N. S. Lewis and H. B. Gray,Evaluation of Pt, Ni, and Ni-Mo electrocatalysts for hydrogen evolution on crystalline Si electrodess *Energy Environ. Sci*, 2011, **4**, 3573-3583.
46. B. Russo and G. Z. Cao,Fabrication and characterization of fluorine-doped thin oxide thin films and nanorod arrays via spray pyrolysiss *Appl. Phys. A*, 2008, **90**, 311-315.

47. L. Yuan, Y. Wang, R. Mema and G. Zhou,Driving force and growth mechanism for spontaneous oxide nanowire formation during the thermal oxidation of metalss *Acta Mater.*, 2011, **59**, 2491-2500.
48. C.-L. M. Cheng, Y.-R.; Chou, M. H.; Huang, C. Y.; Yeh, V.; and S. Y. Wu,Direct observation of short-circuit diffusion during the formation of a single cupric oxide nanowires *Nanotechnology*, 2007, **18**, 245604.
49. A. H. Jayatissa, K. Guo and A. C. Jayasuriya,Fabrication of cuprous and cupric oxide thin films by heat treatments *Appl. Surf. Sci.*, 2009, **255**, 9474-9479.
50. H. K. Cho,Formation of V-Shaped Pits in Nitride Films Grown by Metalorganic Chemical Vapor Depositions *J. Korean Phys. Soc.*, 2003, **42**.
51. A. O. Musa, T. Akomolafe and M. J. Carter,Production of cuprous oxide, a solar cell material, by thermal oxidation and a study of its physical and electrical propertiess *Sol. Energy Mater. Sol. Cells*, 1998, **51**, 305-316.
52. M. S. M. S. Mohd Rafie Johan, Nor Liza Hawari, Hee Ay Ching,Annealing Effects on the Properties of Copper Oxide Thin Films Prepared by Chemical Deposition s *Int. J. Electrochem. Sci.*, , 2011, **6**, 6094 - 6104.
53. G. Gouadec and P. Colomban,Raman Spectroscopy of nanomaterials: How spectra relate to disorder, particle size and mechanical propertiess *Prog. Cryst. Growth Charact. Mater.*, 2007, **53**, 1-56.
54. F. Wu, Y. Myung and P. Banerjee,Unravelling transient phases during thermal oxidation of copper for dense CuO nanowire growths *CrystEngComm*, 2014, **16**, 3264-3267.
55. J. Hou, Z. Wang, C. Yang, H. Cheng, S. Jiao and H. Zhu,Cobalt-bilayer catalyst decorated Ta3N5 nanorod arrays as integrated electrodes for photoelectrochemical water oxidations *Energy Environ. Sci*, 2013, **6**, 3322-3330.
56. E. S. Kim, N. Nishimura, G. Magesh, J. Y. Kim, J.-W. Jang, H. Jun, J. Kubota, K. Domen and J. S. Lee,Fabrication of $CaFe_2O_4$/TaON Heterojunction Photoanode for Photoelectrochemical Water Oxidations *J. Am. Chem. Soc.*, 2013, **135**, 5375-5383.
57. X. Zhang, Y. Liu, S.-T. Lee, S. Yang and Z. Kang,Coupling surface plasmon resonance of gold nanoparticles with slow-photon-effect of TiO_2 photonic crystals for synergistically enhanced photoelectrochemical water splittings *Energy Environ. Sci*, 2014, **7**, 1409-1419.
58. Z. Chen, T. F. Jaramillo, T. G. Deutsch, A. Kleiman-Shwarsctein, A. J. Forman, N. Gaillard, R. Garland, K. Takanabe, C. Heske, M. Sunkara, E. W. McFarland, K. Domen, E. L. Miller, J. A. Turner and H. N. Dinh,Accelerating materials development for photoelectrochemical hydrogen production: Standards for methods, definitions, and reporting protocolss *J. Mater. Res.*, 2010, **25**, 3-16.
59. A. G. Tamirat, W.-N. Su, A. A. Dubale, C.-J. Pan, H.-M. Chen, D. W. Ayele, J.-F. Lee and B.-J. Hwang,Efficient photoelectrochemical water splitting using three dimensional urchin-like hematite nanostructure modified with reduced graphene oxides *J. Power Sources*, 2015, **287**, 119-128.
60. C. Yang, P. D. Tran, P. P. Boix, P. S. Bassi, N. Yantara, L. H. Wong and J. Barber,Engineering a $Cu_2O/NiO/Cu_2MoS_4$ hybrid photocathode for H_2 generation in waters *Nanoscale*, 2014, **6**, 6506-6510.
61. A. G. Tamirat, W.-N. Su, A. A. Dubale, H.-M. Chen and B.-J. Hwang,Photoelectrochemical water splitting at low applied potential using a NiOOH

coated codoped (Sn, Zr) [small alpha]-Fe_2O_3 photoanodes *J. Mater. Chem. A*, 2015, **3**, 5949-5961.

62. E. C. Heltemes,Far-Infrared Properties of Cuprous Oxides *Phys. Rev.*, 1966, **141**, 803-805.
63. L. C. Wang, N. R. de Tacconi, C. R. Chenthamarakshan, K. Rajeshwar and M. Tao,Electrodeposited copper oxide films: Effect of bath pH on grain orientation and orientation-dependent interfacial behaviors *Thin Solid Films*, 2007, **515**, 3090-3095.
64. V. Subramanian, E. E. Wolf and P. V. Kamat,Green Emission to Probe Photoinduced Charging Events in ZnO−Au Nanoparticles. Charge Distribution and Fermi-Level Equilibration†s *J. Phys. Chem. B*, 2003, **107**, 7479-7485.

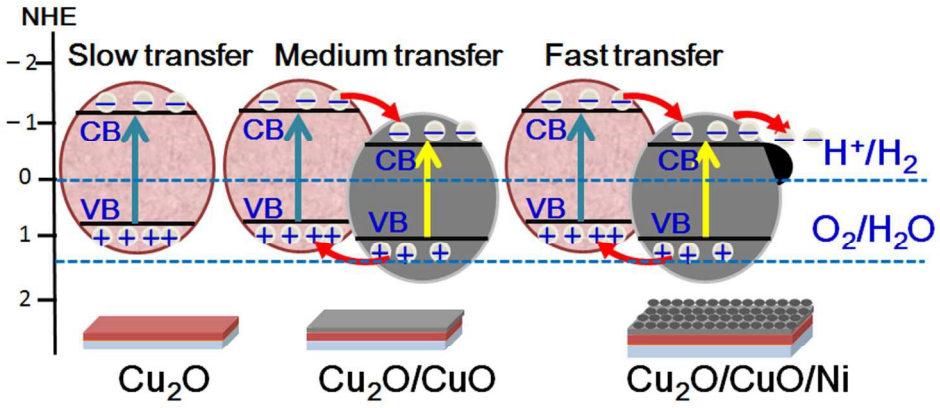

The energy band structure of Cu2O, Cu2O/CuO and Cu2O/CuO/Ni
79x40mm (300 x 300 DPI)